The Astrophysical Journal Supplement Series, 263:35 (21pp), 2022 December https://doi.org/10.3847/1538-4365/ac9c57

R-matrix Electron-impact Excitation Data for the H- and He-like Ions with $Z = 6-30$

Junjie Mao[1,2,3], G. Del Zanna[4], Liyi Gu[5,6], C. Y. Zhang[3], and N. R. Badnell[3]
[1] Department of Astronomy, Tsinghua University, Beijing 100084, People's Republic of China; jmao@tsinghua.edu.cn
[2] Department of Physics, Hiroshima University, 1-3-1 Kagamiyama, HigashiHiroshima, Hiroshima 739-8526, Japan
[3] Department of Physics, University of Strathclyde, Glasgow G4 0NG, UK
[4] Department of Applied Mathematics and Theoretical Physics, University of Cambridge, Cambridge CB3 0WA, UK
[5] SRON Netherlands Institute for Space Research, Niels Bohrweg 4, 2333 CA Leiden, The Netherlands
[6] RIKEN High Energy Astrophysics Laboratory, 2-1 Hirosawa, Wako, Saitama 351-0198, Japan
Received 2022 July 3; revised 2022 October 6; accepted 2022 October 19; published 2022 December 6

Abstract

Plasma models built on extensive atomic data are essential to interpreting observed cosmic spectra. H-like Lyman series and He-like triplets observable in the X-ray band are powerful diagnostic lines to measure the physical properties of various types of astrophysical plasmas. Electron-impact excitation is a fundamental atomic process for the formation of H-like and He-like key diagnostic lines. Electron-impact excitation data adopted by the widely used plasma codes (AtomDB, CHIANTI, and SPEX) do not necessarily agree with each other. Here we present a systematic calculation of electron-impact excitation data of H-like and He-like ions with the atomic number $Z = 6$–30 (i.e., C to Zn). A radiation-damped *R*-matrix intermediate-coupling frame transformation calculation was performed for each ion with configurations up to $n = 6$. We compare the present work with the above three plasma codes and the literature to assess the quality of the new data, which are relevant for current and future high-resolution X-ray spectrometers.

Unified Astronomy Thesaurus concepts: Atomic physics (2063); X-ray astronomy (1810); Atomic spectroscopy (2099)

1. Introduction

X-ray-emitting hot astrophysical plasmas are ubiquitous in the universe: stellar coronae, supernova remnants, hot plasmas in individual galaxies and galaxy assemblies, and the warm–hot intergalactic media along the cosmic web filaments (Kaastra et al. 2017). When these targets are observed with spectrometers on board X-ray space observatories (e.g., Chandra, XMM-Newton, and Suzaku), prominent H- and He-like emission lines from various elements (e.g., O and Fe) often stand out above the continuum (e.g., Paerels & Kahn 2003; Mao et al. 2019). These emission lines are powerful diagnostics tools to constrain the physical properties of the hot astrophysical plasmas, such as temperature, density, elemental abundance, and kinematics.

From the observational perspective, we will soon enter an era with the next generation of X-ray spectrometers, including the X-ray Imaging and Spectroscopy Mission (XRISM, Tashiro et al. 2018, to be launched in early 2023), Advanced Telescope for High Energy Astrophysics (Athena, Nandra et al. 2013, Barret et al. 2018, to be launched in the 2030s), Arcus (Smith et al. 2016, proposed in the USA), Hot Universe Baryon Surveyor (HUBS; Cui et al. 2020, proposed in China), Super-Diffuse Intergalactic Oxygen Surveyor (Super-DIOS; Yamada et al. 2018, proposed in Japan), Colibrí (Heyl et al. 2019, proposed in Canada), and so on.

We had a taste of the future with the Soft X-ray Spectrometers (SXS; Mitsuda et al. 2014) on board Hitomi. When observing the hot ($\sim 4.6 \times 10^7$ K) intracluster media (ICM) of the Perseus galaxy cluster, dozens of emission lines from various ionization stages of cosmically abundant (e.g., Si, Fe, and Ni) and rare (e.g., Cr and Mn) elements are observed. The high-quality line-rich spectrum was used to study the line-of-sight turbulent velocity dispersion (Hitomi Collaboration et al. 2016), the origin of cosmic elements in the ICM (Hitomi Collaboration et al. 2017), the resonance scattering effect of the ICM (Hitomi Collaboration et al. 2018a), and the temperature structure of the ICM (Hitomi Collaboration et al. 2018b).

Astrophysical plasma models play a vital role in interpreting the observed high-resolution X-ray spectra (Raymond 2005; Kaastra et al. 2008). When modeling hot astrophysical plasmas in the collisional ionized equilibrium (CIE), both the APEC (Smith et al. 2001; Foster et al. 2012) model (and its variants) in XSPEC (Arnaud 1996) and the CIE model in SPEX (Kaastra et al. 1996, 2020) are widely used in the community. CHIANTI (Dere et al. 1997; Del Zanna et al. 2021) can also model CIE plasma and it is widely used in the solar community. All these plasma models are built on an extensive yet ever-expanding atomic database. High-quality X-ray spectra from future missions are challenging the plasma models developed since the 1970s (Landini & Monsignori Fossi 1970; Mewe 1972; Raymond & Smith 1977).

When analyzing the same Hitomi/SXS spectra of Perseus using different plasma models (Hitomi Collaboration et al. 2018c), the measured Fe abundance was found to differ by 16%. The systematic uncertainty due to the instrumental effects (e.g., effective area uncertainty and gain correction factor) is within 15%. The statistical uncertainty is, however, about 1%. That is to say, the power of the instrument is not fully exploited. Theoretical atomic calculations and laboratory measurements of the atomic data (e.g., Betancourt-Martinez et al. 2019, 2020; Gu et al. 2019, 2020; Heuer et al. 2021; Shah et al. 2021) are required to bring the results of plasma diagnostics closer.

Table 1
Key Diagnostics Transitions for H-like and He-like Ions

Label	Lower Level	Upper Level
Lyα (H-like)	$1s\ ^2S_{1/2}$	$2p\ ^2P_{3/2,1/2}$
Lyβ (H-like)	$1s\ ^2S_{1/2}$	$3p\ ^2P_{3/2,1/2}$
Lyγ (H-like)	$1s\ ^2S_{1/2}$	$4p\ ^2P_{3/2,1/2}$
Lyδ (H-like)	$1s\ ^2S_{1/2}$	$5p\ ^2P_{3/2,1/2}$
Heα-w (He-like)	$1s^2\ ^1S_0$	$1s\,2p\ ^1P_1$
Heα-x (He-like)	$1s^2\ ^1S_0$	$1s\,2p\ ^3P_2$
Heα-y (He-like)	$1s^2\ ^1S_0$	$1s\,2p\ ^3P_1$
Heα-z (He-like)	$1s^2\ ^1S_0$	$1s\,2s\ ^3S_1$
Heβ-w (He-like)	$1s^2\ ^1S_0$	$1s\,3p\ ^1P_1$
Heγ-w (He-like)	$1s^2\ ^1S_0$	$1s\,4p\ ^1P_1$
Heδ-w (He-like)	$1s^2\ ^1S_0$	$1s\,5p\ ^1P_1$

In this work, we focus on the electron-impact excitation (EIE) data for H- and He-like ions from C to Zn. EIE is one of the fundamental atomic processes in astrophysical plasmas. During the collision between a free electron and an ion, energy can be transferred from the free electron to a bounded electron in the ion, exciting it to an upper energy level. When the excited electron decays back to the lower level via radiative transition, at least one photon is emitted and contributes to the emission lines in the observed spectra.

2. Diagnostic Lines and Line Power

H-like Lyman series and He-like triplets (Table 1) are the key diagnostic lines to measure the physical properties of astrophysical plasmas. These lines are in general strong in the observed spectra (see the review of solar diagnostics by Del Zanna & Mason 2018). We caution that to properly model the observed spectra, dielectronic satellite lines of He-like lines should be included (Dere et al. 2019), which is beyond the scope of this paper.

Lyman series are transitions with $np\ ^2P_{3/2,1/2} \rightarrow 1s\ ^2S_{1/2}$ ($n \geqslant 2$). We mainly focus on Lyα ($n = 2 \rightarrow 1$), Lyβ ($n = 3 \rightarrow 1$), Lyγ ($n = 4 \rightarrow 1$), and Lyδ ($n = 4 \rightarrow 1$) as they are all available in AtomDB, SPEX, and CHIANTI. For a low-density CIE plasma, the Lyα line ($2p\ ^2P_{3/2,1/2} \rightarrow 1s\ ^2S_{1/2}$) should have the highest line power. However, in a high-density CIE plasma, resonance scattering can reduce the intensity of Lyα by scattering a fraction of photons outside our line of sight (Chakraborty et al. 2021, 2022). This will lead to larger ratios of Lyβ/Lyα, Lyγ/Lyα, and Lyδ/Lyα than those in a low-density CIE plasma. On the other hand, at the interface between the hot plasma and cold medium, the charge-exchange process can selectively increase the intensity of, e.g., Lyγ or Lyδ (Gu et al. 2016). This also leads to a larger ratio of Lyβ/Lyα, Lyγ/Lyα, and Lyδ/Lyα than those in a low-density CIE plasma.

A He-like triplet refers to the resonance (allowed) $1s\,2p\ ^1P_1 \rightarrow 1s^2\ ^1S_0$, intercombination (semiforbidden) $1s\,2p\ ^3P_{1,2} \rightarrow 1s^2\ ^1S_0$, and forbidden $1s\,2s\ ^3S_1 \rightarrow 1s^2\ ^1S_0$ transition, respectively. The two intercombination lines are often treated as one line because they are not resolved with current instruments (but will be resolved with future missions). The line ratios among the three are sensitive to plasma temperature and density, external radiation field, and charge-exchange process (Porquet et al. 2010). For a low-density CIE plasma, the resonance line should have the highest line power and the intercombination line have the lowest line power. In a high-density CIE plasma, resonance scattering can on one hand reduce the intensity of the resonance line by scattering a fraction of photons outside our line of sight (e.g., Sazonov et al. 2002; Xu et al. 2002; Ogorzalek et al. 2017; Chen et al. 2018; Hitomi Collaboration et al. 2018c); on the other hand, the intercombination line will be stronger and the forbidden line will be weaker because collisional excitation will depopulate the upper level of the forbidden line to those of the intercombination lines (e.g., Porquet et al. 2010). Furthermore, at the interface between the hot plasma and cold medium, the charge-exchange process can increase the forbidden to resonance line ratio (e.g., Branduardi-Raymont et al. 2007; Zhang et al. 2014; Gu et al. 2016). Similarly, the line ratio of the Heα triplets can also be different from collisionally ionized equilibrium plasma due to photoexcitation (e.g., Porquet et al. 2010). Higher-order resonance (allowed) $1s\,np\ ^1P_1 \rightarrow 1s^2\ ^1S_0$ with $n = 3$–5 can also be present in high-quality spectra of future missions, while other higher-order He-like lines are less observable.

For each optically thin emission line in a CIE plasma, its strength can be described by line power P_{ji} (in photons per unit time and volume):

$$P_{ji}(T,\ n_{\rm H}) = A_{ji}\ n_{\rm H}\ A(Z)\ I(T,\ n_{\rm H})\ N_j(T,\ n_{\rm H}), \qquad (1)$$

where A_{ji} is the spontaneous transition probability from the upper-level j to the lower-level i, $n_{\rm H}$ the hydrogen number density of the plasma, $A(Z)$ the elemental abundance with respect to hydrogen, Z the atomic number, I the normalized ionic fraction (the sum of all the ionization stages of the same element is unity), and N_j the normalized level population of the upper-level j (the sum of all the levels is unity). While the A-value is independent of the plasma temperature, both the ionic fraction (I) and level population (N_j) depend on the plasma temperature and density.

Elemental abundances $A(Z)$ are often given in units of solar abundance and there are quite a few solar abundance tables available to use. Generally speaking, C, N, O, Ne, Mg, Si, S, Ar, Ca, Fe, and Ni are the relatively abundant ones for $Z \geqslant 6$ (Anders & Grevesse 1989; Asplund et al. 2009; Lodders et al. 2009).

The ionic fraction (I) is usually taken from precalculated ionization balance tables, which only depend on the temperature of low-density CIE plasma (Figure 1). The default ionization balance is Bryans et al. (2009) for APEC, Dere et al. (2009) for CHIANTI, and Urdampilleta et al. (2017) for SPEX. Around the peak ionic fraction temperatures, the ionic fraction agrees within a few percent among the three codes. At both higher and lower temperature ends when the ionic fraction is rather small, larger deviations ($\gtrsim$20%) can be found. We caution that metastable levels will start to be populated as the plasma density increases, which can modify the ionization balance significantly (Dufresne & Del Zanna 2019; Dufresne et al. 2020, 2021).

The user can choose which ionization balance and solar abundance table to use in pyatomdb,[7] ChiantiPy,[8] and SPEX. When comparing plasma models, it is better to use the same solar abundance and ionization balance tables.

The level population (N_j) depends on various atomic processes. Figure 2 illustrates the percentage contribution of the atomic processes to the level population of Si XIV and Si XIII for a CIE plasma with $kT = 1$ keV. Similar results can be

[7] https://github.com/AtomDB/pyatomdb
[8] https://github.com/chianti-atomic/ChiantiPy

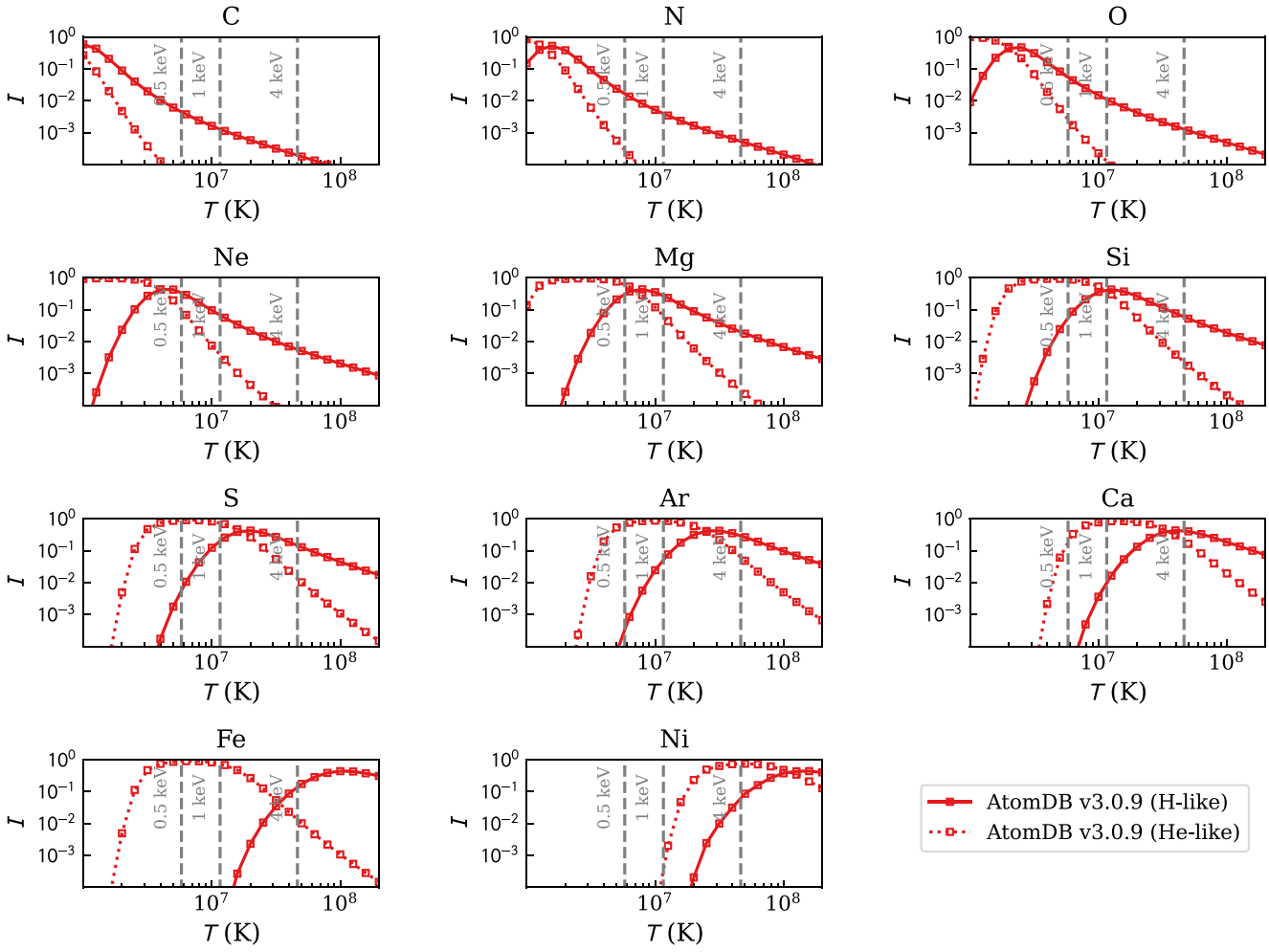

Figure 1. Ionic fraction (I) for cosmically abundant metals in CIE plasmas based on Bryans et al. (2009) as the default of AtomDB v3.0.9. The red solid and dashed lines are for H- and He-like ions, respectively. Vertical gray dashed lines mark the typical temperatures of hot plasmas in individual galaxies (∼0.5 keV, dotted), groups of galaxies (∼1 keV, dashed), and clusters of galaxies (∼4 keV, dotted–dashed), respectively.

found for other H- and He-like ions in CIE plasmas. Generally speaking, EIE contributes most to the upper-level population of resonance lines. Radiative recombination (RR) has a minor contribution to the level population. Note that the same RR data, sourced from Badnell (2006), are implemented via interpolation for AtomDB and CHIANTI or parameterization (Mao & Kaastra 2016) for SPEX. The contribution from a cascade is negligible for resonance lines but it can be crucial for forbidden lines (Hitomi Collaboration et al. 2018c).

3. Status Quo

We examine EIE data in the latest versions of AtomDB (v3.0.9), CHIANTI (v10.0.1), and SPEX (v3.06.01). The EIE data of the key diagnostics line (Table 1) are sourced differently in the three atomic databases. For H-like ions, AtomDB mainly adopts the distorted waves data (with the independent process and isolated resonances approximation) of Li et al. (2015) for elements heavier than and including Al. For lighter elements, either R-matrix data (Ballance et al. 2003) or a distorted-wave calculation by A. Foster with the Flexible Atomic Code (FAC; Gu 2008) are used. For CHIANTI and SPEX, R-matrix data are used for a few ions. Interpolation or extrapolation along the isoelectronic sequence is used for the rest of the H-like ions. Table 2 provides a summary of the source of the EIE data of the Lyα to Lyδ transitions in the three atomic databases.

For He-like ions, AtomDB mainly adopts R-matrix data (including the radiation-damping effect) for all the levels up to $n = 5$: Whiteford et al. (2001) for He-like Fe XXV and Whiteford (2005) for other He-like ions. The latter ones, available on OPEN-ADAS,[9] were calculated following Whiteford et al. (2001), for He-like Ar and Fe only) with some modifications (given in the comment section of the data files). These data are not validated (e.g., comparing to previous calculations) in a peer-reviewed journal publication as the lead author left the field before finishing the project. In particular, the He-like Fe XXV data of Whiteford (2005) is not consistent with that of Whiteford et al. (2001). This is described in Section 5 later. CHIANTI also uses a large fraction of these data (Whiteford 2005). But it uses the R-matrix data (without the radiation-damping effect) of Aggarwal et al. (2009) for Na X and interpolation along the isoelectronic sequence for P XIV and K XVIII. SPEX adopts the Coulomb–Born exchange data of Sampson et al. (1983), which ignored resonances.

EIE data are usually provided in the form of dimensionless effective collisional strength (Υ_{ij}). This is obtained by

[9] https://open.adas.ac.uk/

Table 2
Source of the EIE Data of the H-like Lyα to Lyδ Transitions in SPEX v3.06.01, AtomDB v3.0.9, and CHIANTI Database v10.0.1

Ion	SPEX	AtomDB	CHIANTI
C VI	Aggarwal & Kingston (1991a, RM)	Ballance et al. (2003, RM)	Ballance et al. (2003, RM)
N VII	Interpolation	FAC (DW)	Interpolation
O VIII	Interpolation	Ballance et al. (2003, RM)	Ballance et al. (2003, RM)
Ne X	Aggarwal & Kingston (1991b, RM), DW for Lyβ	Ballance et al. (2003, RM)	Ballance et al. (2003, RM)
Na XI	Interpolation	FAC (DW)	Interpolation
Mg XII	Interpolation	FAC (DW)	Interpolation
Al XIII	Interpolation	Li et al. (2015, DW)	Interpolation
Si XIV	Aggarwal & Kingston (1992a, RM)	Li et al. (2015, DW)	Aggarwal & Kingston (1992a, RM)
P XV	Interpolation	Li et al. (2015, DW)	Interpolation
S XVI	Interpolation	Li et al. (2015, DW)	Interpolation
Cl XVII	Interpolation	Li et al. (2015, DW)	Interpolation
Ar XVIII	Interpolation	Li et al. (2015, DW)	Interpolation
K XIX	Interpolation	Li et al. (2015, DW)	Interpolation
Ca XX	Aggarwal & Kingston (1992b, RM)	Li et al. (2015, DW)	Aggarwal & Kingston (1992b, RM)
Cr XXIV	Interpolation	Li et al. (2015, DW)	⋯
Mn XXV	Interpolation	Li et al. (2015, DW)	⋯
Fe XXVI	Kisielius et al. (1996, RM), interpolation for Ly δ	Li et al. (2015, DW)	Ballance et al. (2002, RM)
Ni XXVIII	Extrapolation	Li et al. (2015, DW)	Extrapolation

Note. DW and RM are short for distorted-wave and *R*-matrix calculations, respectively.

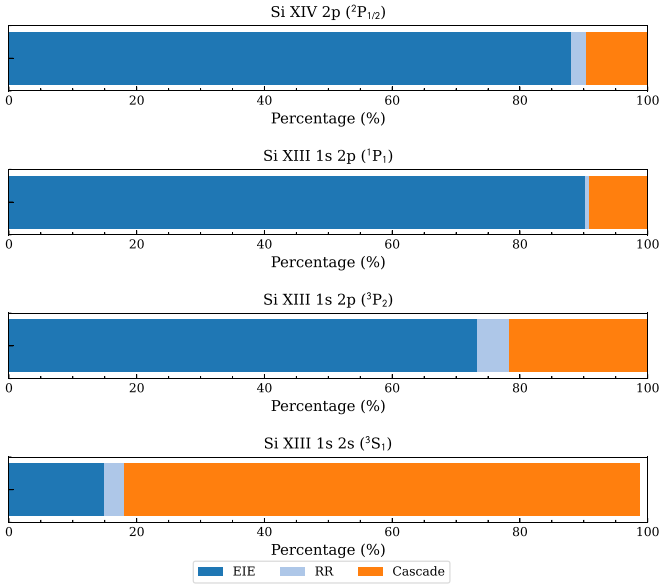

Figure 2. Percentage contribution of the atomic processes to the level population of Si XIV and Si XIII in a CIE plasma with $kT = 1$ keV. The four levels, from top to bottom, are the upper levels of Lyα, Heα-w, Heα-x, and Heα-z. Contributions from the electron-impact excitation (EIE), radiative recombination (RR), and cascade are shown in dark blue, light blue, and orange. The SPEX code (v3.06.01) is used to calculate the level population here.

convolving the ordinary collision strength (Ω_{ij}) with the Maxwellian distribution:

$$\Upsilon_{ij} = \int_0^\infty \Omega_{ij} \exp\left(-\frac{E_f}{kT}\right) d\left(\frac{E_f}{kT}\right), \quad (2)$$

where E_f is the scattered electron energy, k the Boltzmann constant, and T the electron temperature of the plasma. Effective collisional strength is usually tabulated on a narrow or wide temperature grid, depending on the original calculations. Interpolation among these temperatures and extrapolation beyond the temperature range are implemented by AtomDB and CHIANTI. For SPEX, the collision data as a function of temperature are implemented via parameterization to cover a wide temperature range (Kaastra et al. 2008).

We caution that the energy levels and spontaneous transition rate (i.e., *A*-values) among these three atomic databases do not necessarily agree. Detailed comparisons are given in the Appendix.

4. *R*-matrix Calculation

Here we present a systematic *R*-matrix calculation for H- and He-like ions. An *R*-matrix intermediate-coupling frame transformation (ICFT; Griffin et al. 1998) calculation including the effect of radiation damping (Robicheaux et al. 1995; Gorczyca & Badnell 1996) was performed for each ion with configurations up to $n = 6$. That is to say, 36 levels for H-like ions and 71 levels for He-like ions.

We used the AUTOSTRUCTURE code (Badnell 2011) to calculate the target atomic structure. Wave functions were obtained by diagonalizing the Breit–Pauli Hamiltonian (Eissner et al. 1974). We include one-body relativistic terms (mass-velocity, nuclear plus Blume and Watson spin–orbit, and Darwin) perturbatively. The Thomas–Fermi–Dirac–Amaldi model was used for the electronic potential with *nl*-dependent scaling parameters (Nussbaumer & Storey 1978). We set the *nl*-dependent scaling parameters to unity, following Ballance et al. (2002) and Malespin et al. (2011).

For the scattering calculation, we used the radiation-damped *R*-matrix ICFT method. We used 110 continuum basis orbitals for H- and He-like ions with configurations up to $n = 6$ to cover the energy range from the ground state to $\gtrsim 6\, I_p$, where I_p is the ionization threshold. This ensures the cross section is close to the asymptotic limit before extrapolating to the infinite limit point.

Angular momenta up to $2J = 26$ and $2J = 96$ were included for the exchange and nonexchange calculations, respectively. Higher angular momenta (up to infinity) were included following the top-up formula of the Burgess sum rule (Burgess 1974) for dipole-allowed transitions and a geometric

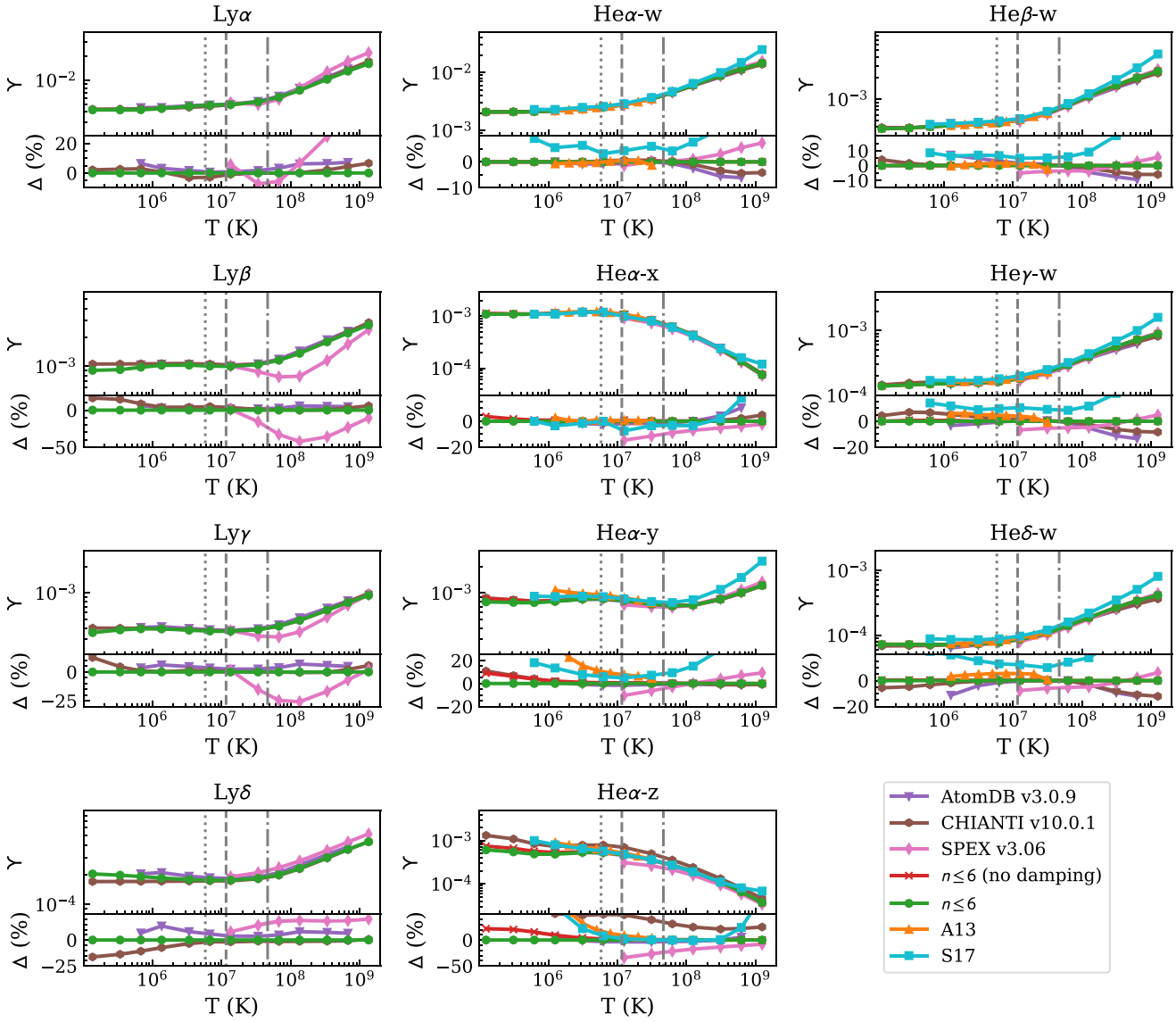

Figure 3. Comparison of effective collisional strength data of key diagnostic lines for Fe XXVI and Fe XXV. AtomDB, CHIANTI, and SPEX data are shown in purple (triangle down), brown (hexagon), and magenta (diamond), respectively. The present work without radiation damping, the present work with radiation damping, Aggarwal & Keenan (2013), and Si et al. (2017) are shown in red (x), green (circle), orange (triangle up), and cyan (square), respectively. The percentage difference (Δ) is given with respect to the present work. Vertical dashed lines mark typical temperatures of hot plasmas in individual galaxies ($\sim$0.5 keV, dotted), groups of galaxies ($\sim$1 keV, dashed), and clusters of galaxies ($\sim$4 keV, dotted–dashed), respectively. When the ionic fraction is too low (Figure 1), SPEX skipped the level population calculation (including the effective collisional strength data) for computational efficiency.

series for the non-dipole-allowed transitions (Badnell & Griffin 2001).

The outer-region exchange calculation of the resonance region used a rather fine energy mesh with the number of sampling points ranging from $\sim 1.0 \times 10^5$ for H-like C VI to $\sim 5.8 \times 10^5$ for H-like Zn XXX and from $\sim 0.8 \times 10^5$ for He-like C V to 5.6×10^5 for He-like Zn XXXIX. Beyond the resonance regions (up to 6 times the ionization potential), the outer-region exchange calculations were performed with a coarse energy mesh with $\sim$2500 sampling points. A similar coarse energy mesh was also used for the outer-region nonexchange calculations.

To complete the Maxwellian convolution (Equation (2)) at high temperatures, we calculated the infinite-energy Born and dipole line strength limits using AUTOSTRUCTURE. Between the last calculated energy point and the two limits, interpolation was used according to the type of transition in the Burgess–Tully scaled domain (i.e., the quadrature of the reduced collision strength over reduced energy; see Burgess & Tully 1992).

5. Results

We have obtained radiation-damped R-matrix EIE data for the H- and He-like isoelectronic sequence with $Z = 6$–30, where Z is the atomic number, e.g., $Z = 14$ for silicon. Our effective collision strengths cover 4 orders of magnitude in temperature $(z+1)^2(2 \times 10^2,\ 2 \times 10^6)$ K, where z is the ionic charge (e.g., $z = 10$ for He-like Mg XI).

Effective collision strength data are archived according to the Atomic Data and Analysis Structure (ADAS) data class *adf04* and are available on Zenodo at doi:10.5281/zenodo.7226828. Optimal interval-averaged ordinary collision strength data are also provided, which can be used for convolution with

Table 3
Source of the EIE Data of the He-like Triplet Transitions in SPEX v3.06.01, AtomDB v3.0.9, and CHIANTI Database v9.0.1

Ion	SPEX	AtomDB	CHIANTI
C V	Sampson et al. (1983, CBE)	Whiteford (2005, RM)	Interpolation
N VI	Sampson et al. (1983, CBE)	Whiteford (2005, RM)	Interpolation
O VII	Sampson et al. (1983, CBE)	Whiteford (2005, RM)	Whiteford (2005, RM)
Ne IX	Sampson et al. (1983, CBE)	Whiteford (2005, RM)	Whiteford (2005, RM)
Na X	Sampson et al. (1983, CBE)	Whiteford (2005, RM)	Aggarwal et al. (2009)
Mg XI	Sampson et al. (1983, CBE)	Whiteford (2005, RM)	Whiteford (2005, RM)
Al XII	Sampson et al. (1983, CBE)	Whiteford (2005, RM)	Whiteford (2005, RM)
Si XIII	Sampson et al. (1983, CBE)	Whiteford (2005, RM)	Whiteford (2005, RM)
P XIV	Sampson et al. (1983, CBE)	Whiteford (2005, RM)	Interpolation
S XV	Sampson et al. (1983, CBE)	Whiteford (2005, RM)	Whiteford (2005, RM)
Cl XVI	Sampson et al. (1983, CBE)	Whiteford (2005, RM)	Interpolation
Ar XVII	Sampson et al. (1983, CBE)	Whiteford (2005, RM)	Whiteford (2005, RM)
K XVIII	Sampson et al. (1983, CBE)	Whiteford (2005, RM)	Interpolation
Ca XIX	Sampson et al. (1983, CBE)	Whiteford (2005, RM)	Whiteford (2005, RM)
Cr XXIII	Sampson et al. (1983, CBE)	Whiteford (2005, RM)	Whiteford (2005, RM)
Mn XXIV	Sampson et al. (1983, CBE)	Whiteford (2005, RM)	...
Fe XXV	Sampson et al. (1983, CBE)	(Whiteford et al. 2001, RM)	Whiteford (2005, RM)
Ni XXVII	Sampson et al. (1983, CBE)	Whiteford (2005, RM)	Whiteford (2005, RM)

Note. Sampson et al. (1983) and Whiteford (2005) used Coulomb–Born-Exchange and *R*-matrix methods, respectively.

non-Maxwellian distributions. The ordinary collision strength data files are produced with the latest version of adasexj.[10] For each transition, the number of bins (or intervals) is around 100, depending on the width of the resonance region. Moreover, the Zenodo package also includes the input files of the *R*-matrix calculations, binned ordinary collision strength data (in the *adf04* format), atomic data, and python scripts used to create the figures presented in this article. These data will be used to improve the atomic databases of astrophysical plasma codes, such as AtomDB (Smith et al. 2001; Foster et al. 2012), CHIANTI (Dere et al. 1997; Del Zanna et al. 2021), and SPEX (Kaastra et al. 1996, 2020).

6. Discussion

A scattering calculation using the *R*-matrix ICFT method (Section 4) necessarily uses the Breit–Pauli *R*-matrix structure code. This includes only one-body relativistic operators (excluding quantum electrodynamics (QED)).[11] In addition, it requires the user to supply a unique set of nonrelativistic orthogonal radial orbitals from an external atomic structure code. Our atomic structure calculated with AUTOSTRUCTURE for subsequent *R*-matrix scattering calculations is denoted as AS-RM. When compared with other structure calculations (including AUTOSTRUCTURE) which make use of two-body relativistic operators and/or QED and/or nonunique and/or nonorthogonal relativistic orbitals, the AS-RM level energies and *A*-values are less accurate. For the upper levels of the key diagnostic transitions (Table 1), the AS-RM level energies can differ up to ∼0.05% for H-like and ∼0.23% for He-like when compared to the three atomic databases (see the Appendix). Similarly, by $n = 5$ the AS-RM *A*-values can differ by up to ∼25% for H-like and ∼40% for He-like while the *A*-values of the key transitions among the three databases differ by up to ∼5% for H-like and ∼40% (see the Appendix). More accurate level energies and *A*-values than the AS-RM ones can be obtained from AUTOSTRUCTURE as described in the Appendix and we denote them AS-REL. Other sources include Aggarwal et al. (2009, 2010), Aggarwal & Keenan (2010, 2012a, 2012b, 2013), and Malespin et al. (2011).

In this section, we compare the effective collisional strength of the key diagnostic lines in Table 1 among the present work, all three atomic databases (AtomDB, CHIANTI, and SPEX), and some reference results not incorporated in the three atomic databases. We focus on the following representative elements: Fe (Section 6.1), Ca (Section 6.2), Si (Section 6.3), and O (Section 6.4). We also show exemplary impacts on observations (Section 6.5).

6.1. Fe XXVI and Fe XXV

As shown in Figure 3, the effective collision strength of the Lyman series agrees $\lesssim$5% of the time for Lyα and $\lesssim$20% of the time for Lyβ to Lyδ among the present work, AtomDB, CHIANTI, and Aggarwal & Keenan (2013). Lyα to Lyγ data in SPEX can differ by $\gtrsim$50% from the other data sets at $T > 10^7$ K. The original Dirac *R*-matrix calculation by Kisielius et al. (1996) was performed at $T = 10^{6-7.5}$ K. Hence, the root of the difference is in the extrapolation at $T > 10^{7.5}$ K in SPEX. Lyδ in SPEX is obtained from interpolation along the isoelectronic sequence (Table 3), which is systematically higher (up to ∼20%) than the present work.

For the Heα-w (resonance) line, all *R*-matrix data agree $\lesssim$3% of the time at $T < 10^8$ K. Distorted-wave data (with independent process and isolated resonance approximation, IPIRDW) from Si et al. (2017) is systematically higher by a few percent. Such an offset is also shown in Figure 2 of Si et al. (2017), where the authors calculated both IPIRDW and Dirac *R*-matrix data. The offset is due to the different treatment of resonances by the two calculations, which is illustrated in Figure 1 of Si et al. (2017). At $T > 10^8$ K, IPIRDW data by Si et al. (2017) increases more rapidly than the *R*-matrix data. The difference originates from the convolution of a Maxwellian (Equation (2)) at high temperatures (see Section 4 and Si et al. 2017). The comparison of Heβ to Heδ resonance transitions

[10] http://www.apap-network.org/codes/serial/misc/adasexj.f
[11] Breit and QED interactions are absent also from the structure used by the Dirac *R*-matrix code.

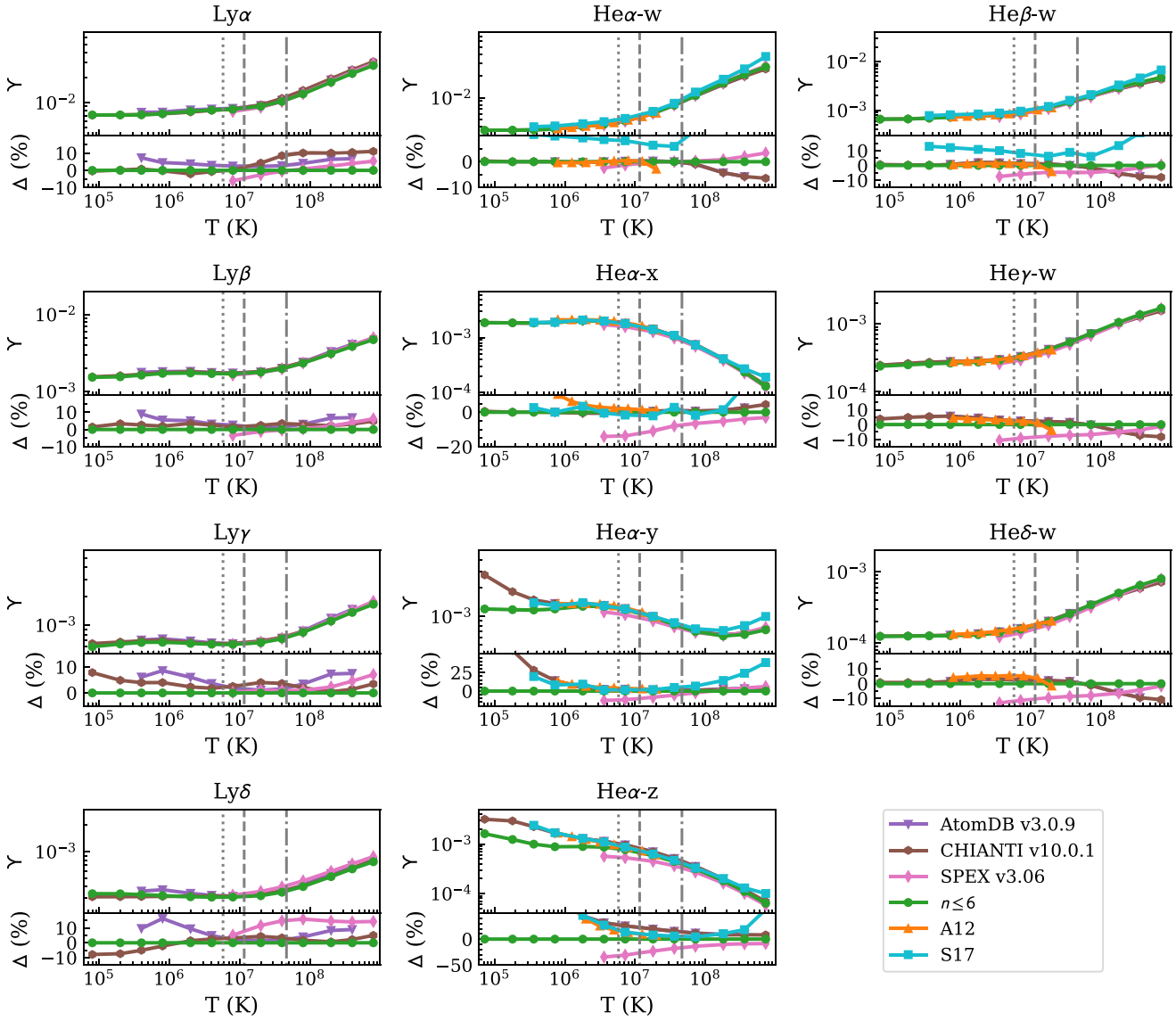

Figure 4. Comparison of effective collisional strength data of key diagnostic lines for Ca XX and Ca XIX. AtomDB, CHIANTI, and SPEX data are shown in purple (triangle down), brown (hexagon), and magenta (diamond), respectively. The present work, Aggarwal & Keenan (2012b), and Si et al. (2017) are shown in green (circle), orange (triangle up), and cyan (square), respectively. Percentage difference (Δ) is given with respect to the present work. Vertical dashed lines mark typical temperatures of hot plasmas in individual galaxies (∼0.5 keV, dotted), groups of galaxies (∼1 keV, dashed), and clusters of galaxies (∼4 keV, dotted–dashed), respectively. When the ionic fraction is too low (Figure 1), SPEX skipped the level population calculation (including the effective collisional strength data) for computational efficiency.

among different data sets share similar issues to those found for Heα.

For the Heα-x (intercombination) line, all R-matrix data agree $\lesssim$3% of the time at $T < 10^8$ K. IPIRDW data from Si et al. (2017) agrees $\lesssim$8% of the time. For the Heα-y (intercombination) line, relatively large differences ($\lesssim$25%) can be found among different data sets at $T < 10^7$ K. The present work and Whiteford et al. (2001, used by AtomDB) agree $\lesssim$3% at $T \sim 10^{6-7}$ K (the latter does not calculate below $\sim 10^6$ K). Whiteford (2005) covers 1 order of magnitude lower in temperature than Whiteford et al. (2001) but differs by up to ∼15%. Between Si et al. (2017) and Aggarwal & Keenan (2013), the former is relatively lower (see also Figure 2 of Si et al. 2017). At $T = 5.8 \times 10^6$ K (or 0.5 keV), Aggarwal & Keenan (2013) is larger by ∼12% than the present work.

Similarly, large differences are found below 5.8×10^6 K for the Heα-z (forbidden) line. Furthermore, Whiteford (2005) data is systematically above ($\gtrsim$20%) all other calculations at $T \lesssim 10^8$ K. At $T \sim 10^6$ K, Whiteford (2005) is larger than both Whiteford et al. (2001) and the present work by ∼50%. Such a large difference cannot be explained by the radiation-damping effect, which is $\lesssim$20% at low temperatures and has no impact at higher temperatures (Figure 3).

For both Heα-y and z lines, the data from Aggarwal & Keenan (2013) and Si et al. (2017) are larger ($\gtrsim$10%) than the present work at $T \lesssim 5.8 \times 10^6$ K (or $T \lesssim 0.5$ keV). On the one hand, radiation damping is not included in Aggarwal & Keenan (2013). On the other hand, all the calculations are subject to the inherent lack of convergence in the target configuration-interaction expansion and/or the collisional close-coupling expansion for weaker transitions (Fernández-Menchero et al. 2017; Del Zanna et al. 2019). Note that, under CIE conditions, the ionic fraction of Fe XXV at $T \lesssim 0.5$ keV is more than 3 orders of magnitude lower than the peak value (Figure 1).

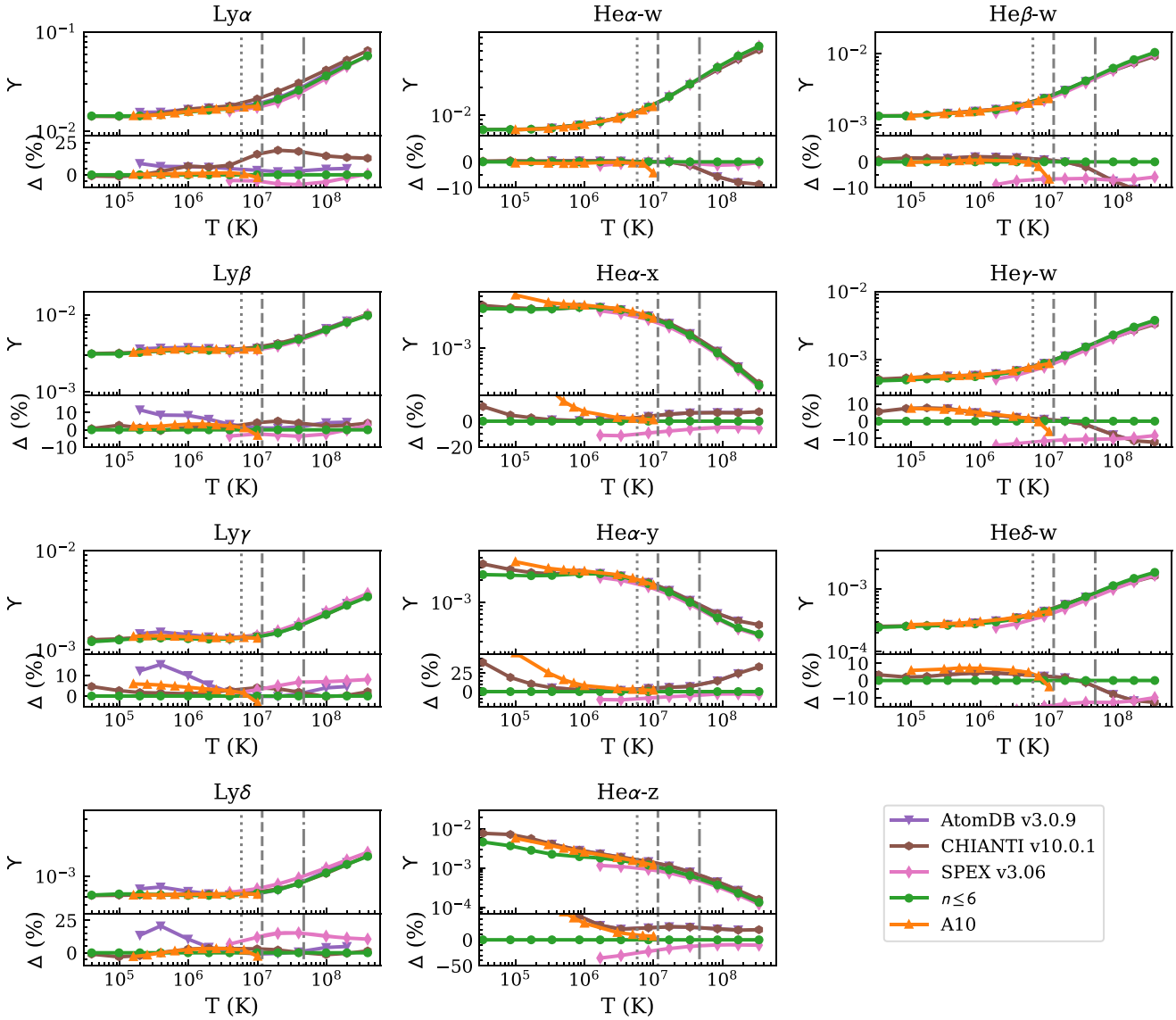

Figure 5. Comparison of effective collisional strength data of key diagnostic lines for Si XIV and Si XIII. AtomDB, CHIANTI, and SPEX data are shown in purple (triangle down), brown (hexagon), and magenta (diamond), respectively. The present work and Aggarwal & Keenan (2010) are shown in green (circle) and orange (triangle up), respectively. Percentage difference (Δ) is given with respect to the present work. Vertical dashed lines mark typical temperatures of hot plasmas in individual galaxies (∼0.5 keV, dotted), groups of galaxies (∼1 keV, dashed), and clusters of galaxies (∼4 keV, dotted–dashed), respectively. When the ionic fraction is too low (Figure 1), SPEX skipped the level population calculation (including the effective collisional strength data) for computational efficiency.

6.2. Ca XX and Ca XIX

As shown in Figure 4, the effective collision strengths of the Lyman series agree $\lesssim$10% of the time for Lyα to Lyδ lines between the present work and Aggarwal & Kingston (1992b; used by CHIANTI and SPEX). Similar good agreement is found between the present work and Li et al. (2015, used by AtomDB) at $T \gtrsim 10^7$ K. At lower temperatures, relatively larger differences (up to ∼20%) can be found.

For the Heα-w (resonance) line, all R-matrix data agree $\lesssim$3% at $T < 10^8$ K except CHIANTI at $T \gtrsim 10^8$ K. The original R-matrix data from Aggarwal & Keenan (2012b) is calculated up to $10^{7.4}$ K. The high-temperature extrapolation in CHIANTI might be the issue. IPIRDW data from Si et al. (2017) is systematically higher by $\gtrsim$5%, similar to Fe XXV (Section 6.1). For the Heα-x (intercombination) line, the Sampson et al. (1983) data (used by SPEX) stands out at $T \sim 10^{7-8}$ K but it is still within ∼20%. For the Heα-y (intercombination) line, large differences ($\gtrsim$25%) can be found between the present work and Whiteford (2005, used by AtomDB and CHIANTI) at $T \lesssim 10^6$ K. Even larger differences can be found for the Heα-z line at $T \lesssim 10^6$ K, although the ionic fraction of Ca XIX at $T \lesssim 10^{6.2}$ K is more than 3 orders of magnitude lower than the peak value under CIE conditions (Figure 1). Again, Whiteford (2005) is larger than the present work by ∼10% at high temperatures ($T \gtrsim 10^8$ K). For Heβ lines, the SPEX Heβ-z data is again systematically larger than all other calculations at $T \gtrsim 10^7$ K.

The comparison of Heβ to Heδ resonance transitions among different data sets share similar issues found for Heα-w with one caveat. The Heγ-w and Heδ-w data in Si et al. (2017) are systematically lower by 1–3 orders of magnitude (beyond the plotting frame of Figure 4) when compared to all the R-matrix data.

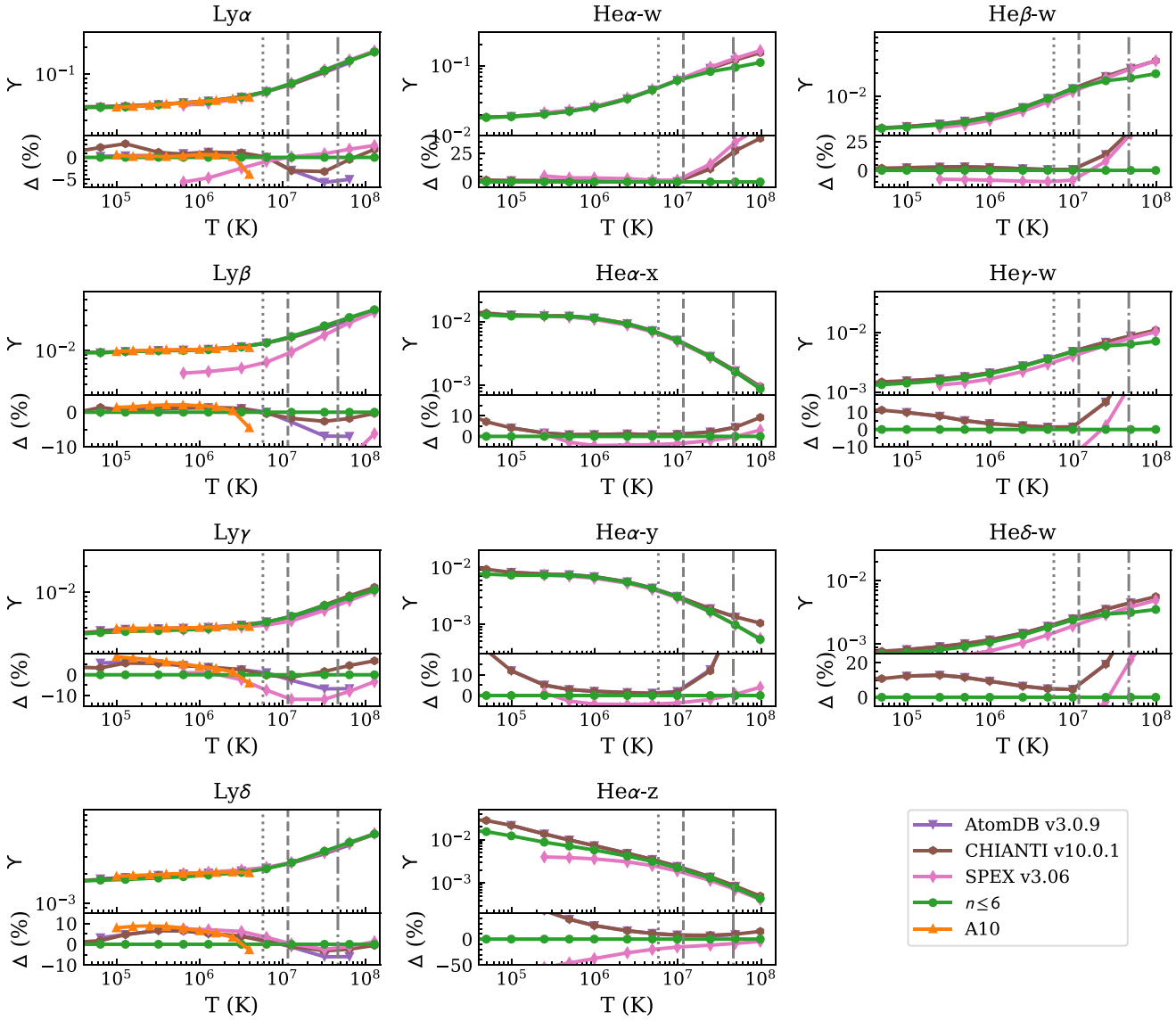

Figure 6. Comparison of effective collisional strength data of key diagnostic lines for O VIII and O VII. AtomDB, CHIANTI, and SPEX data are shown in purple (hexagon), brown (diamond), and magenta (triangle down), respectively. The present work and Aggarwal et al. (2010) are shown in green (circle) and yellow (triangle up), respectively. Percentage difference (Δ) is given with respect to the present work. Vertical dashed lines mark typical temperatures of hot plasmas in individual galaxies (∼0.5 keV, dotted), groups of galaxies (∼1 keV, dashed), and clusters of galaxies (∼4 keV, dotted–dashed), respectively. When the ionic fraction is too low (Figure 1), SPEX skipped the level population calculation (including the effective collisional strength data) for computational efficiency.

6.3. Si XIV and Si XIII

As shown in Figure 5, Lyα to Lyδ agree $\lesssim$5% among all *R*-matrix data sets, while the IPIRDW data from Li et al. (2015) show relatively large (but still within ∼25%) differences. The high-temperature extrapolation by CHIANTI and SPEX above $10^{6.4}$ K (Aggarwal & Kingston 1992a) might explain the difference noticed here.

For Heα and Heδ lines, apart from similar issues discussed above, we notice the relatively large ($\gtrsim$20%) increase of Whiteford (2005, used by CHIANTI) at $T > 10^8$ K for the Heα-y line. There is no high-temperature extrapolation here because the original calculation goes to 4.5×10^8 K. At such a high temperature, the ionic fraction of Si XIII is more than 3 orders of magnitude lower than the peak value under CIE conditions (Figure 1).

6.4. O VIII and O VII

As shown in Figure 6, the effective collision strengths of the Lyman series agree $\lesssim$ 5% for Lyα and Lyβ and $\lesssim$ 10% for Lyγ and Lyδ among the present work, AtomDB, CHIANTI, and Aggarwal et al. (2010). The original data of Ballance et al. (2003) was calculated up to 1.8×10^7 K. At this boundary temperature, the Ballance et al. (2003) data is $\lesssim$5% lower than the present work. This smaller difference is likely due to the coverage of scattering energy in the two calculations. Ballance et al. (2003) used 70 continuum basis orbitals to cover at least ∼4.5 times the ionization potential of O VIII. In the present work, we used 110 continuum basis orbitals to cover at least ∼6.2 times the ionization potential. As shown in Figure 3 of Malespin et al. (2011), covering a wider energy range can better constrain the high-temperature effective collision

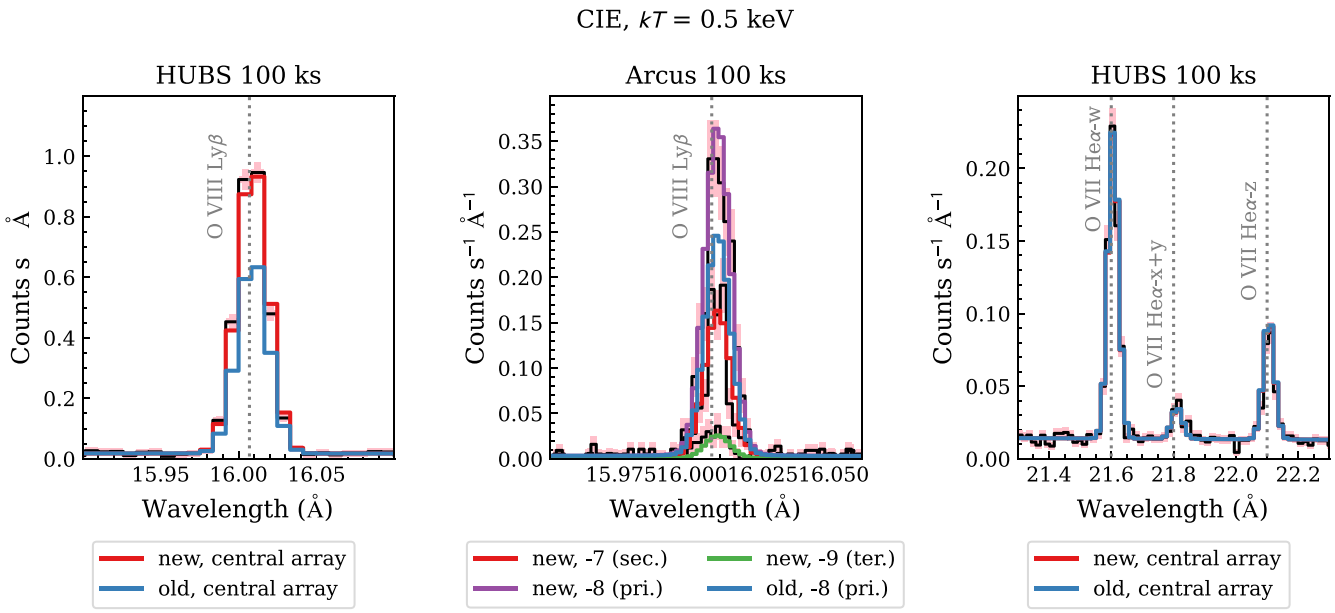

Figure 7. Simulated HUBS (left and right) and Arcus (middle) spectra in the O VIII Lyβ (left and middle) and O VII triplet neighborhood. Simulated data are shown in black and the 1σ statistical uncertainties in pink. Model spectra using the new atomic data presented in this work are shown with dashed lines, while those using the atomic data from SPEX v3.06.01 are shown with solid blue lines. Due to geometry overlapping for Arcus, the O VIII Lyβ line comes from the primary spectral order (the −8th order, purple) as well as two neighboring spectral orders (−7th and −9th). See the text for the detailed simulation setup (Section 6.4).

strength. At $T \gtrsim 1.8 \times 10^7$ K, AtomDB and CHIANTI extrapolated the high-temperature data differently. In addition, the SPEX Lyβ data is systematically lower than the present work by $\gtrsim$10% at $T \lesssim 10^8$ K.

Differences of more than ∼10% are found between the present work and Whiteford (2005) for the resonance and intercombination lines at $T \gtrsim 4 \times 10^7$ K. Under CIE conditions, the ionic fraction of O VII at $T \gtrsim 10^7$ K is more than 3 orders of magnitude lower than the peak value (Figure 1). For the forbidden line (Heα-z), a $\gtrsim$10% difference is noticed at $T < 10^6$ K, where the ionic fraction of O VII peaks. This temperature is less relevant for studies of individual galaxies and galaxy assemblies, but it might be relevant for stellar coronae.

6.5. Exemplary Impact to Observations

As mentioned earlier, a relatively large difference ($\gtrsim$10% for $T \lesssim 10^8$ K) is found between the present work and SPEX v3.06.01 for O VIII Lyβ, which is less affected by resonance scattering than Lyα. Here we show simulated spectra representative of two next-generation high-resolution X-ray spectrometers: HUBS (Cui et al. 2020) and Arcus (Smith et al. 2016). The former employs superconducting transition-edge sensors while the latter adopts critical-angle transmission gratings to achieve rather high spectral resolution. The central array of HUBS aims to yield an energy resolution of 0.6 eV in the 0.1–2 keV energy band. Arcus will achieve $R = \lambda/\Delta\lambda = 3800$ in the 10–50 Å wavelength range when using a very narrow extraction region. Furthermore, the relatively large effective area of both instruments enables observers to obtain high-quality spectra for relatively dim targets (as in the following example).

For both instruments, we set an arbitrary exposure time of 100 ks, an observed 0.5–10 keV flux of 5.0×10^{-12} erg s^{-1} cm^{-2}, a negligible line-of-sight Galactic hydrogen column density of 1.0×10^{20} cm^{-2}, and a single-temperature CIE plasma with $kT = 0.5$ keV. Only the oxygen abundance is set to solar (Lodders et al. 2009) while other metal abundances are set to zero. We used SPEX v3.06.01 (the latest released version) for the simulation, as well as a development version where the H- and He-like electron-impact excitation data were updated using the present work. As shown in the left panel of Figure 7, the old atomic data would underestimate the O VIII Lyβ line flux at the core by ∼32%, which is a factor of ∼8 times larger than the 1σ statistical uncertainty in this HUBS simulation.[12] In the Arcus simulation,[13] the O VIII Lyβ comes from three geometrical overlapping spectral orders: the −8th order (primary), the −7th order (secondary), and −9th order (tertiary). The flux difference between the old and new atomic data for the primary spectral order is a factor of ∼6 larger than the flux of the tertiary spectral order. For the O VII triplet, as shown in the right panel of Figure 7, the line flux between the old and new atomic data are negligible. The old and new atomic atomic data agree well at $kT = 0.5$ keV for the resonance and intercombination lines (Figure 6), thus we do not expect noticeable differences in the simulated spectra. The old and new atomic data of the forbidden line differ by ∼20% at $kT = 0.5$ keV (Figure 6). But its impact is limited because cascading from upper levels contributes most to the level population (Figure 2).

7. Summary

We have presented systematic radiation-damped R-matrix intermediate-coupling frame transformation calculations of EIE data of H- and He-like ions with atomic number $Z = 6$–30. For each ion, fine-structure energy levels up to $n = 6$ (36 levels for H-like ions and 71 levels for He-like ions) were included in the target configuration-interaction and close-coupling collision expansion. Level-resolved effective collision strengths were

[12] We use the HUBS response files (v20201227) of the central array, which has a energy resolution of 0.6 eV.

[13] We use the Arcus response files (6500d8b) with the "osip60" configuration, which has a better energy resolution but a smaller effective area.

obtained among these levels over 4 orders of magnitude in temperature. When compared with existing *R*-matrix or distorted-wave data in the atomic databases and literature, generally speaking, relatively good agreements can be found near the peak temperatures of charge state distribution under collisional ionized equilibrium conditions. The new data calculated here are relevant for current and future high-resolution X-ray spectrometers such as the upcoming XRISM in 2023, Athena/X-IFU, HUBS, Arcus, and so on around the 2030s.

We thank the referees for a careful reading of the manuscript and constructive suggestions to improve the quality of the work. J.M. acknowledges useful discussions with Adam Foster, Connor Ballance, Martin O Mullane, Zhu Liu, Guiyun Liang, Mingyue Hao, Ran Si, and Jelle Kaastra. G.D.Z. acknowledges support from STFC (UK) via the consolidated grant to the atomic astrophysics group at DAMTP, University of Cambridge (ST/T000481/1). This work is supported by STFC (UK) through the University of Strathclyde UK APAP network grants ST/T000481/1 and ST/V000863/1.

Appendix
Level Energies and *A*-values of H- and He-like Key Diagnostic Lines

Accurate level energies are essential to obtaining the correct rest-frame line energy (or wavelength). The level energies of the upper levels of the key diagnostics lines in Table 1 agree well among the three databases with only a few exceptions (Tables 4 and 5). For H-like ones, the largest difference comes from the level energy of Ar XVIII 2p ($^2P_{1/2}$) in CHIANTI (taken from Phillips et al. 2003), which is lower than AtomDB/SPEX by 0.4 eV. For He-like ones, the largest difference comes from the level energy of Mg XI 1s 3p $^1P_1$ in SPEX, which is lower by 0.7 eV than AtomDB/CHIANTI. This can be comparable to the energy gain correction of the instrument, as shown in the analysis of the Hitomi/SXS spectrum of the Perseus galaxy cluster (Hitomi Collaboration et al. 2018a). The derived bulk velocity of the intracluster media differs by 6 km s^{-1} between SPEX v3.03 and AtomDB v3.0.8, while the energy gain correction of the instrument is 14 km s^{-1}.

As discussed in Section 6, the AS-RM energy levels are less accurate than those that can be obtained from AUTOSTRUCTURE without the restrictions imposed by their use by the Breit–Pauli *R*-matrix code. The latter is denoted as AS-REL. The AS-REL energy levels are also shown in Tables 4 and 5. For H-like ions, the inclusion by AUTOSTRUCTURE of the QED effects (vacuum polarization and electron self-energy) reduce the inaccuracy from $\lesssim$0.05% to $\lesssim$0.001% when compared with the three atomic databases. For He-like ions at low charge the two-body Coulomb interaction is the main source of uncertainty ($\lesssim$0.23% when compared with the three atomic databases), while at high charge relativistic effects are the main source and the inclusion as well by AUTOSTRUCTURE of the two-body relativistic interactions reduces the overall inaccuracy (from $\lesssim$0.15% to $\lesssim$0.03% for Ni XXVII when compared with the three atomic databases).

As shown in Table 6, for the $np\,^2P_{3/2,1/2}$, $n = 2$–5 energy levels in H-like ions, the *A*-values in AtomDB, CHIANTI, and SPEX agree well ($\lesssim$5%) for the resonance lines. Larger deviations (up to 40%) can be found for energy levels in He-like ions (Table 7), especially the upper levels of some intercombination lines and forbidden lines.

The *A*-values shown in Tables 6 and 7 can differ by up to ∼40%, depending on which databases are compared. For instance, the *A*-value of the C V Heα-y line differs between AS-RM and SPEX by ∼40%, while the AS-RM and AtomDB values are identical. The *A*-value for this transition in CHIANTI is ∼27% larger than the AS-RM/AtomDB ones. We are limited to using nonrelativistic orbitals (by our scattering calculation) but the perturbative one-body relativistic operators (mass-velocity and Darwin) become increasingly large as the ion charge increases and imbalance the level mixing that in turn leads to the relatively low accuracy for the AS-RM Heγ-w and Heδ-w transition rates of high-*Z* elements. Using (kappa-averaged) relativistic orbitals in AUTOSTRUCTURE eliminates the perturbative imbalance. This can be seen most clearly for H-like ions (where the databases agree well). The AS-RM Ni XXVIII Lyδ *A*-values in Table 6 are ∼20% smaller than the database ones. AUTOSTRUCTURE calculations using relativistic orbitals reduce the difference to a few percent, depending on the database. These transitions are shown in the last columns of Tables 6 and 7. The corresponding Ni XXVII Heγ-w, Heδ-w transition rates now agree with CHIANTI to within 3%. Both the AS-RM and AS-REL data sets (in the *adf04* format) are available in the Zenodo package.

Table 4
Energy Levels (in eV) of H-like Ions in SPEX v3.06.01, AtomDB v3.0.9, and CHIANTI Database v10.0.1

Ion	Level	SPEX	AtomDB	CHIANTI	AS-RM	AS-REL
C VI	$2p\ ^2P_{1/2}$	367.5	367.5 (−0.0)	367.5 (−0.0)	367.5	367.5
C VI	$2p\ ^2P_{3/2}$	367.5	367.5 (−0.0)	367.5 (−0.0)	367.6	367.6
C VI	$3p\ ^2P_{1/2}$	435.5	435.5 (−0.0)	435.5 (−0.0)	435.6	435.6
C VI	$3p\ ^2P_{3/2}$	435.6	435.6 (−0.0)	435.6 (−0.0)	435.6	435.6
C VI	$4p\ ^2P_{1/2}$	459.4	459.4 (−0.0)	459.4 (−0.0)	459.4	459.4
C VI	$4p\ ^2P_{3/2}$	459.4	459.4 (−0.0)	459.4 (−0.0)	459.4	459.4
C VI	$5p\ ^2P_{1/2}$	470.4	470.4 (−0.0)	470.4 (−0.0)	470.4	470.4
C VI	$5p\ ^2P_{3/2}$	470.4	470.4 (−0.0)	470.4 (−0.0)	470.4	470.4
N VII	$2p\ ^2P_{1/2}$	500.2	500.2 (−0.0)	500.2 (−0.0)	500.3	500.3
N VII	$2p\ ^2P_{3/2}$	500.4	500.4 (−0.0)	500.4 (−0.0)	500.4	500.4
N VII	$3p\ ^2P_{1/2}$	592.9	592.9 (−0.0)	592.9 (−0.0)	593.0	593.0
N VII	$3p\ ^2P_{3/2}$	593.0	593.0 (−0.0)	593.0 (−0.0)	593.0	593.0
N VII	$4p\ ^2P_{1/2}$	625.4	625.4 (−0.0)	625.4 (−0.0)	625.4	625.4
N VII	$4p\ ^2P_{3/2}$	625.4	625.4 (−0.0)	625.4 (−0.0)	625.4	625.4
N VII	$5p\ ^2P_{1/2}$	640.4	640.4 (−0.0)	640.4 (−0.0)	640.4	640.4
N VII	$5p\ ^2P_{3/2}$	640.4	640.4 (−0.0)	640.4 (−0.0)	640.4	640.4
O VIII	$2p\ ^2P_{1/2}$	653.5	653.5 (−0.0)	653.5 (−0.0)	653.6	653.5
O VIII	$2p\ ^2P_{3/2}$	653.7	653.7 (−0.0)	653.7 (−0.0)	653.8	653.7
O VIII	$3p\ ^2P_{1/2}$	774.6	774.6 (−0.0)	774.6 (−0.0)	774.7	774.6
O VIII	$3p\ ^2P_{3/2}$	774.6	774.6 (−0.0)	774.6 (−0.0)	774.7	774.7
O VIII	$4p\ ^2P_{1/2}$	817.0	817.0 (−0.0)	817.0 (−0.0)	817.0	817.0
O VIII	$4p\ ^2P_{3/2}$	817.0	817.0 (−0.0)	817.0 (−0.0)	817.1	817.0
O VIII	$5p\ ^2P_{1/2}$	836.6	836.6 (−0.0)	836.6 (−0.0)	836.7	836.6
O VIII	$5p\ ^2P_{3/2}$	836.6	836.6 (−0.0)	836.6 (−0.0)	836.7	836.6
Ne X	$2p\ ^2P_{1/2}$	1021.4	1021.5 (+0.1)	1021.5 (+0.1)	1021.7	1021.5
Ne X	$2p\ ^2P_{3/2}$	1021.9	1022.0 (+0.1)	1022.0 (+0.1)	1022.1	1022.0
Ne X	$3p\ ^2P_{1/2}$	1210.8	1210.8 (−0.0)	1210.8 (−0.0)	1211.0	1210.9
Ne X	$3p\ ^2P_{3/2}$	1210.9	1211.0 (+0.1)	1211.0 (+0.1)	1211.1	1211.0
Ne X	$4p\ ^2P_{1/2}$	1277.0	1277.1 (+0.1)	1277.1 (+0.1)	1277.3	1277.1
Ne X	$4p\ ^2P_{3/2}$	1277.1	1277.1 (+0.1)	1277.1 (+0.1)	1277.3	1277.2
Ne X	$5p\ ^2P_{1/2}$	1307.7	1307.7 (+0.1)	1307.7 (+0.1)	1307.9	1307.8
Ne X	$5p\ ^2P_{3/2}$	1307.7	1307.8 (+0.1)	1307.8 (+0.1)	1307.9	1307.8
Na XI	$2p\ ^2P_{1/2}$	1236.3	1236.3 (−0.0)	1236.3 (−0.0)	1236.5	1236.3
Na XI	$2p\ ^2P_{3/2}$	1237.0	1237.0 (−0.0)	1237.0 (−0.0)	1237.2	1237.0
Na XI	$3p\ ^2P_{1/2}$	1465.5	1465.5 (−0.0)	1465.5 (−0.0)	1465.7	1465.5
Na XI	$3p\ ^2P_{3/2}$	1465.7	1465.7 (−0.0)	1465.7 (−0.0)	1465.9	1465.7
Na XI	$4p\ ^2P_{1/2}$	1545.7	1545.7 (−0.0)	1545.7 (−0.0)	1545.9	1545.7
Na XI	$4p\ ^2P_{3/2}$	1545.8	1545.8 (−0.0)	1545.8 (−0.0)	1546.0	1545.8
Na XI	$5p\ ^2P_{1/2}$	1582.8	1582.8 (−0.0)	1582.8 (−0.0)	1583.0	1582.8
Na XI	$5p\ ^2P_{3/2}$	1582.8	1582.8 (−0.0)	1582.8 (−0.0)	1583.1	1582.9
Mg XII	$2p\ ^2P_{1/2}$	1471.7	1471.7 (+0.0)	1471.7 (+0.0)	1472.0	1471.7
Mg XII	$2p\ ^2P_{3/2}$	1472.6	1472.6 (+0.0)	1472.6 (+0.0)	1472.9	1472.7
Mg XII	$3p\ ^2P_{1/2}$	1744.6	1744.6 (+0.0)	1744.6 (+0.0)	1744.9	1744.6
Mg XII	$3p\ ^2P_{3/2}$	1744.8	1744.8 (+0.0)	1744.8 (+0.0)	1745.2	1744.9
Mg XII	$4p\ ^2P_{1/2}$	1840.0	1840.0 (+0.0)	1840.0 (+0.0)	1840.3	1840.1
Mg XII	$4p\ ^2P_{3/2}$	1840.1	1840.1 (+0.0)	1840.1 (+0.0)	1840.5	1840.2
Mg XII	$5p\ ^2P_{1/2}$	1884.2	1884.2 (+0.0)	1884.2 (+0.0)	1884.5	1884.2
Mg XII	$5p\ ^2P_{3/2}$	1884.3	1884.3 (+0.0)	1884.3 (+0.0)	1884.6	1884.3
Al XIII	$2p\ ^2P_{1/2}$	1727.7	1727.7 (+0.0)	1727.7 (+0.0)	1728.1	1727.7
Al XIII	$2p\ ^2P_{3/2}$	1729.0	1729.0 (+0.0)	1729.0 (+0.0)	1729.4	1729.0
Al XIII	$3p\ ^2P_{1/2}$	2048.1	2048.1 (+0.0)	2048.1 (+0.0)	2048.5	2048.1
Al XIII	$3p\ ^2P_{3/2}$	2048.5	2048.5 (+0.0)	2048.5 (+0.0)	2048.9	2048.5
Al XIII	$4p\ ^2P_{1/2}$	2160.2	2160.2 (+0.0)	2160.2 (+0.0)	2160.6	2160.2
Al XIII	$4p\ ^2P_{3/2}$	2160.3	2160.3 (+0.0)	2160.3 (+0.0)	2160.7	2160.4
Al XIII	$5p\ ^2P_{1/2}$	2212.0	2212.0 (+0.0)	2212.0 (+0.0)	2212.4	2212.1
Al XIII	$5p\ ^2P_{3/2}$	2212.1	2212.1 (+0.0)	2212.1 (+0.0)	2212.5	2212.2
Si XIV	$2p\ ^2P_{1/2}$	2004.3	2004.3 (+0.0)	2004.3 (+0.0)	2004.8	2004.4
Si XIV	$2p\ ^2P_{3/2}$	2006.1	2006.1 (+0.0)	2006.1 (+0.0)	2006.6	2006.1
Si XIV	$3p\ ^2P_{1/2}$	2376.1	2376.1 (+0.0)	2376.1 (+0.0)	2376.6	2376.2
Si XIV	$3p\ ^2P_{3/2}$	2376.6	2376.6 (+0.0)	2376.6 (+0.0)	2377.1	2376.7
Si XIV	$4p\ ^2P_{1/2}$	2506.2	2506.2 (+0.0)	2506.2 (+0.0)	2506.7	2506.2
Si XIV	$4p\ ^2P_{3/2}$	2506.4	2506.4 (+0.0)	2506.4 (+0.0)	2506.9	2506.4
Si XIV	$5p\ ^2P_{1/2}$	2566.3	2566.3 (+0.0)	2566.3 (+0.0)	2566.8	2566.4
Si XIV	$5p\ ^2P_{3/2}$	2566.4	2566.4 (+0.0)	2566.4 (+0.0)	2566.9	2566.5

Table 4
(Continued)

Ion	Level	SPEX	AtomDB	CHIANTI	AS-RM	AS-REL
P XV	$2p\ ^2P_{1/2}$	2301.6	2301.6 (+0.0)	2301.6 (+0.0)	2302.3	2301.7
P XV	$2p\ ^2P_{3/2}$	2304.0	2304.0 (+0.0)	2304.0 (+0.0)	2304.6	2304.0
P XV	$3p\ ^2P_{1/2}$	2728.7	2728.7 (+0.0)	2728.7 (+0.0)	2729.3	2728.7
P XV	$3p\ ^2P_{3/2}$	2729.4	2729.4 (+0.0)	2729.4 (+0.0)	2730.0	2729.4
P XV	$4p\ ^2P_{1/2}$	2878.0	2878.0 (+0.0)	2878.0 (+0.0)	2878.7	2878.1
P XV	$4p\ ^2P_{3/2}$	2878.3	2878.3 (+0.0)	2878.3 (+0.0)	2879.0	2878.4
P XV	$5p\ ^2P_{1/2}$	2947.1	2947.1 (+0.0)	2947.1 (+0.0)	2947.8	2947.2
P XV	$5p\ ^2P_{3/2}$	2947.3	2947.3 (+0.0)	2947.3 (+0.0)	2947.9	2947.3
S XVI	$2p\ ^2P_{1/2}$	2619.7	2619.7 (+0.0)	2619.7 (+0.0)	2620.5	2619.7
S XVI	$2p\ ^2P_{3/2}$	2622.7	2622.7 (+0.0)	2622.7 (+0.0)	2623.4	2622.7
S XVI	$3p\ ^2P_{1/2}$	3105.9	3105.9 (+0.0)	3105.9 (+0.0)	3106.6	3105.9
S XVI	$3p\ ^2P_{3/2}$	3106.7	3106.7 (+0.0)	3106.7 (+0.0)	3107.5	3106.8
S XVI	$4p\ ^2P_{1/2}$	3275.9	3275.9 (+0.0)	3275.9 (+0.0)	3276.7	3275.9
S XVI	$4p\ ^2P_{3/2}$	3276.3	3276.3 (+0.0)	3276.3 (+0.0)	3277.0	3276.3
S XVI	$5p\ ^2P_{1/2}$	3354.5	3354.5 (+0.0)	3354.5 (+0.0)	3355.3	3354.6
S XVI	$5p\ ^2P_{3/2}$	3354.7	3354.7 (+0.0)	3354.7 (+0.0)	3355.5	3354.8
Cl XVII	$2p\ ^2P_{1/2}$	2958.5	2958.5 (+0.0)	2958.5 (−0.0)	2959.5	2958.6
Cl XVII	$2p\ ^2P_{3/2}$	2962.3	2962.4 (+0.0)	2962.3 (−0.0)	2963.3	2962.4
Cl XVII	$3p\ ^2P_{1/2}$	3507.7	3507.7 (+0.0)	3507.7 (−0.0)	3508.6	3507.8
Cl XVII	$3p\ ^2P_{3/2}$	3508.8	3508.8 (+0.0)	3508.8 (−0.0)	3509.8	3508.9
Cl XVII	$4p\ ^2P_{1/2}$	3699.8	3699.8 (+0.0)	3699.8 (−0.0)	3700.7	3699.8
Cl XVII	$4p\ ^2P_{3/2}$	3700.2	3700.2 (+0.0)	3700.2 (−0.0)	3701.2	3700.3
Cl XVII	$5p\ ^2P_{1/2}$	3788.6	3788.6 (+0.0)	3788.6 (−0.0)	3789.5	3788.7
Cl XVII	$5p\ ^2P_{3/2}$	3788.8	3788.8 (+0.0)	3788.8 (−0.0)	3789.8	3788.9
Ar XVIII	$2p\ ^2P_{1/2}$	3318.2	3318.2 (+0.0)	3317.7 (−0.4)	3319.3	3318.2
Ar XVIII	$2p\ ^2P_{3/2}$	3323.0	3323.0 (+0.0)	3323.1 (+0.1)	3324.1	3323.0
Ar XVIII	$3p\ ^2P_{1/2}$	3934.3	3934.3 (+0.0)	3934.3 (+0.0)	3935.4	3934.3
Ar XVIII	$3p\ ^2P_{3/2}$	3935.7	3935.7 (+0.0)	3935.7 (+0.0)	3936.8	3935.8
Ar XVIII	$4p\ ^2P_{1/2}$	4149.7	4149.7 (+0.0)	4149.7 (+0.0)	4150.8	4149.8
Ar XVIII	$4p\ ^2P_{3/2}$	4150.3	4150.3 (+0.0)	4150.3 (+0.0)	4151.4	4150.4
Ar XVIII	$5p\ ^2P_{1/2}$	4249.4	4249.4 (+0.0)	4249.4 (+0.0)	4250.5	4249.4
Ar XVIII	$5p\ ^2P_{3/2}$	4249.7	4249.7 (+0.0)	4249.7 (+0.0)	4250.8	4249.7
K XIX	$2p\ ^2P_{1/2}$	3698.7	3698.7 (+0.0)	3698.7 (+0.0)	3700.0	3698.7
K XIX	$2p\ ^2P_{3/2}$	3704.7	3704.7 (+0.0)	3704.7 (+0.0)	3705.9	3704.7
K XIX	$3p\ ^2P_{1/2}$	4385.7	4385.7 (+0.0)	4385.7 (+0.0)	4387.0	4385.7
K XIX	$3p\ ^2P_{3/2}$	4387.4	4387.4 (+0.0)	4387.4 (+0.0)	4388.7	4387.5
K XIX	$4p\ ^2P_{1/2}$	4625.8	4625.9 (+0.0)	4625.9 (+0.0)	4627.2	4625.9
K XIX	$4p\ ^2P_{3/2}$	4626.6	4626.6 (+0.0)	4626.6 (+0.0)	4627.9	4626.7
K XIX	$5p\ ^2P_{1/2}$	4736.9	4736.9 (+0.0)	4736.9 (+0.0)	4738.2	4737.0
K XIX	$5p\ ^2P_{3/2}$	4737.3	4737.3 (+0.0)	4737.3 (+0.0)	4738.6	4737.4
Ca XX	$2p\ ^2P_{1/2}$	4100.1	4100.1 (+0.0)	4100.1 (+0.0)	4101.7	4100.2
Ca XX	$2p\ ^2P_{3/2}$	4107.5	4107.5 (+0.0)	4107.5 (+0.0)	4109.0	4107.6
Ca XX	$3p\ ^2P_{1/2}$	4861.9	4861.9 (+0.0)	4861.9 (+0.0)	4863.5	4862.0
Ca XX	$3p\ ^2P_{3/2}$	4864.1	4864.1 (+0.0)	4864.1 (+0.0)	4865.6	4864.2
Ca XX	$4p\ ^2P_{1/2}$	5128.2	5128.2 (+0.0)	5128.2 (+0.0)	5129.8	5128.3
Ca XX	$4p\ ^2P_{3/2}$	5129.1	5129.2 (+0.0)	5129.2 (+0.0)	5130.7	5129.2
Ca XX	$5p\ ^2P_{1/2}$	5251.4	5251.4 (+0.0)	5251.4 (+0.0)	5252.9	5251.5
Ca XX	$5p\ ^2P_{3/2}$	5251.8	5251.8 (+0.0)	5251.8 (+0.0)	5253.3	5251.9
Cr XXIV	$2p\ ^2P_{1/2}$	5916.4	5916.5 (+0.1)	⋯	5919.1	5916.5
Cr XXIV	$2p\ ^2P_{3/2}$	5931.8	5931.9 (+0.1)	⋯	5934.3	5931.9
Cr XXIV	$3p\ ^2P_{1/2}$	7017.2	7017.3 (+0.1)	⋯	7019.9	7017.3
Cr XXIV	$3p\ ^2P_{3/2}$	7021.7	7021.8 (+0.1)	⋯	7024.3	7021.9
Cr XXIV	$4p\ ^2P_{1/2}$	7401.8	7401.9 (+0.1)	⋯	7404.5	7402.0
Cr XXIV	$4p\ ^2P_{3/2}$	7403.8	7403.8 (+0.1)	⋯	7406.3	7403.9
Cr XXIV	$5p\ ^2P_{1/2}$	7579.6	7579.7 (+0.1)	⋯	7582.2	7579.8
Cr XXIV	$5p\ ^2P_{3/2}$	7580.6	7580.7 (+0.1)	⋯	7583.1	7580.7
Mn XXV	$2p\ ^2P_{1/2}$	6423.5	6423.6 (+0.1)	⋯	6426.5	6423.5
Mn XXV	$2p\ ^2P_{3/2}$	6441.6	6441.7 (+0.1)	⋯	6444.4	6441.7
Mn XXV	$3p\ ^2P_{1/2}$	7619.1	7619.1 (+0.1)	⋯	7622.0	7619.2
Mn XXV	$3p\ ^2P_{3/2}$	7624.4	7624.5 (+0.1)	⋯	7627.2	7624.6
Mn XXV	$4p\ ^2P_{1/2}$	8036.8	8036.8 (+0.1)	⋯	8039.7	8036.9
Mn XXV	$4p\ ^2P_{3/2}$	8039.0	8039.1 (+0.1)	⋯	8041.9	8039.2
Mn XXV	$5p\ ^2P_{1/2}$	8229.8	8229.9 (+0.1)	⋯	8232.7	8229.9
Mn XXV	$5p\ ^2P_{3/2}$	8230.9	8231.0 (+0.1)	⋯	8233.8	8231.1

Table 4
(Continued)

Ion	Level	SPEX	AtomDB	CHIANTI	AS-RM	AS-REL
Fe XXVI	$2p\ ^2P_{1/2}$	6951.9	6952.0 (+0.1)	6952.0 (+0.1)	6955.2	6951.9
Fe XXVI	$2p\ ^2P_{3/2}$	6973.1	6973.2 (+0.1)	6973.2 (+0.1)	6976.2	6973.2
Fe XXVI	$3p\ ^2P_{1/2}$	8246.3	8246.4 (+0.1)	8246.4 (+0.1)	8249.6	8246.5
Fe XXVI	$3p\ ^2P_{3/2}$	8252.6	8252.7 (+0.1)	8252.7 (+0.1)	8255.7	8252.8
Fe XXVI	$4p\ ^2P_{1/2}$	8698.5	8698.6 (+0.1)	8698.6 (+0.1)	8701.7	8698.7
Fe XXVI	$4p\ ^2P_{3/2}$	8701.1	8701.2 (+0.1)	8701.2 (+0.1)	8704.3	8701.3
Fe XXVI	$5p\ ^2P_{1/2}$	8907.4	8907.5 (+0.1)	8907.5 (+0.1)	8910.6	8907.6
Fe XXVI	$5p\ ^2P_{3/2}$	8908.8	8908.9 (+0.1)	8908.9 (+0.1)	8911.9	8908.9
Ni XXVIII	$2p\ ^2P_{1/2}$	8073.0	8073.1 (+0.1)	8073.1 (+0.1)	8077.1	8073.0
Ni XXVIII	$2p\ ^2P_{3/2}$	8101.6	8101.7 (+0.1)	8101.7 (+0.1)	8105.3	8101.8
Ni XXVIII	$3p\ ^2P_{1/2}$	9577.4	9577.6 (+0.1)	9577.6 (+0.1)	9581.5	9577.6
Ni XXVIII	$3p\ ^2P_{3/2}$	9585.9	9586.1 (+0.1)	9586.1 (+0.1)	9589.6	9586.1
Ni XXVIII	$4p\ ^2P_{1/2}$	10,102.8	10,103.0 (+0.1)	10,103.0 (+0.1)	10,106.7	10,103.0
Ni XXVIII	$4p\ ^2P_{3/2}$	10,106.4	10,106.5 (+0.1)	10,106.5 (+0.1)	10,110.1	10,106.6
Ni XXVIII	$5p\ ^2P_{1/2}$	10,345.5	10,345.6 (+0.1)	10,345.6 (+0.1)	10,349.4	10,345.7
Ni XXVIII	$5p\ ^2P_{3/2}$	10,347.3	10,347.5 (+0.1)	10,347.5 (+0.1)	10,351.1	10,347.6

Note. The numbers in the parentheses are the differences (in eV) with respect to SPEX of the other two databases. The penultimate column shows the results of the present AUTOSTRUCTURE calculations which were used for the *R*-matrix calculations (AS-RM). The last column shows the results of AUTOSTRUCTURE calculations including relativistic effects (AS-REL) that are necessarily omitted by AS-RM. See the discussion in Section 6 and the Appendix.

Table 5
Energy Levels (in eV) of He-like Ions in SPEX v3.06.01, AtomDB v3.0.9, and CHIANTI Database v10.0.1

Ion	Level	SPEX	AtomDB	CHIANTI	AS-RM	AS-REL
C V	$1s\ 2p\ ^1P_1$	307.9	307.9 (+0.0)	307.9 (+0.0)	308.6	308.5
C V	$1s\ 2p\ ^3P_2$	304.4	304.4 (+0.0)	304.4 (+0.0)	304.5	304.5
C V	$1s\ 2p\ ^3P_1$	304.4	304.4 (+0.0)	304.4 (+0.0)	304.5	304.4
C V	$1s\ 2s\ ^3S_1$	299.0	299.0 (+0.0)	299.0 (+0.0)	299.0	298.9
C V	$1s\ 3p\ ^1P_1$	354.5	354.5 (−0.0)	354.5 (−0.0)	354.9	354.8
C V	$1s\ 4p\ ^1P_1$	370.9	370.9 (−0.0)	370.9 (−0.0)	371.3	371.2
C V	$1s\ 5p\ ^1P_1$	378.5	378.5 (−0.0)	378.5 (−0.0)	378.9	378.8
N VI	$1s\ 2p\ ^1P_1$	430.7	430.7 (−0.0)	430.7 (+0.0)	431.4	431.3
N VI	$1s\ 2p\ ^3P_2$	426.3	426.3 (−0.0)	426.3 (−0.0)	426.5	426.3
N VI	$1s\ 2p\ ^3P_1$	426.3	426.3 (−0.0)	426.3 (−0.0)	426.4	426.3
N VI	$1s\ 2s\ ^3S_1$	419.8	419.8 (−0.0)	419.8 (−0.0)	419.9	419.8
N VI	$1s\ 3p\ ^1P_1$	498.0	498.0 (−0.0)	498.0 (−0.0)	498.4	498.3
N VI	$1s\ 4p\ ^1P_1$	521.6	521.6 (−0.0)	521.6 (−0.0)	522.0	521.8
N VI	$1s\ 5p\ ^1P_1$	532.6	532.6 (+0.0)	532.6 (+0.0)	532.9	532.8
O VII	$1s\ 2p\ ^1P_1$	573.9	573.9 (−0.0)	574.0 (+0.0)	574.8	574.6
O VII	$1s\ 2p\ ^3P_2$	568.6	568.6 (−0.0)	568.7 (+0.1)	568.9	568.7
O VII	$1s\ 2p\ ^3P_1$	568.6	568.6 (−0.0)	568.6 (+0.1)	568.9	568.7
O VII	$1s\ 2s\ ^3S_1$	561.0	561.0 (−0.0)	561.1 (+0.1)	561.2	561.0
O VII	$1s\ 3p\ ^1P_1$	665.6	665.6 (−0.0)	665.6 (−0.0)	666.1	665.9
O VII	$1s\ 4p\ ^1P_1$	697.8	697.8 (−0.0)	697.8 (−0.0)	698.3	698.1
O VII	$1s\ 5p\ ^1P_1$	712.7	712.7 (−0.0)	712.7 (−0.0)	713.2	713.0
Ne IX	$1s\ 2p\ ^1P_1$	922.0	922.0 (−0.0)	922.0 (−0.0)	923.1	922.7
Ne IX	$1s\ 2p\ ^3P_2$	915.0	915.0 (−0.0)	915.0 (−0.0)	915.5	914.9
Ne IX	$1s\ 2p\ ^3P_1$	914.8	914.8 (−0.0)	914.8 (−0.0)	915.2	914.8
Ne IX	$1s\ 2s\ ^3S_1$	905.1	905.1 (−0.0)	905.1 (−0.0)	905.5	905.0
Ne IX	$1s\ 3p\ ^1P_1$	1073.8	1073.8 (−0.0)	1073.8 (−0.0)	1074.6	1074.1
Ne IX	$1s\ 4p\ ^1P_1$	1127.1	1127.1 (−0.0)	1127.1 (−0.0)	1127.8	1127.3
Ne IX	$1s\ 5p\ ^1P_1$	1151.8	1151.8 (−0.0)	1151.8 (−0.0)	1152.5	1152.0
Na X	$1s\ 2p\ ^1P_1$	1126.9	1126.9 (+0.0)	1126.9 (−0.0)	1128.1	1127.5
Na X	$1s\ 2p\ ^3P_2$	1119.0	1119.0 (+0.0)	1119.0 (+0.0)	1119.6	1118.9
Na X	$1s\ 2p\ ^3P_1$	1118.7	1118.7 (+0.0)	1118.7 (−0.0)	1119.3	1118.6
Na X	$1s\ 2s\ ^3S_1$	1107.8	1107.8 (+0.0)	1107.8 (−0.0)	1108.4	1107.8
Na X	$1s\ 3p\ ^1P_1$	1314.4	1314.4 (−0.0)	1314.4 (−0.0)	1315.3	1314.7
Na X	$1s\ 4p\ ^1P_1$	1380.2	1380.2 (+0.0)	1380.2 (+0.0)	1381.1	1380.5
Na X	$1s\ 5p\ ^1P_1$	1410.8	1410.8 (−0.0)	1410.8 (−0.0)	1411.6	1411.0
Mg XI	$1s\ 2p\ ^1P_1$	1352.2	1352.2 (+0.0)	1352.2 (+0.0)	1353.8	1353.0
Mg XI	$1s\ 2p\ ^3P_2$	1343.5	1343.5 (+0.0)	1343.5 (+0.0)	1344.4	1343.4
Mg XI	$1s\ 2p\ ^3P_1$	1343.1	1343.1 (+0.0)	1343.1 (+0.0)	1343.9	1343.0
Mg XI	$1s\ 2s\ ^3S_1$	1331.1	1331.1 (+0.0)	1331.1 (+0.0)	1331.9	1331.0
Mg XI	$1s\ 3p\ ^1P_1$	1580.0	1579.3 (−0.7)	1579.3 (−0.7)	1580.5	1579.6

Table 5
(Continued)

Ion	Level	SPEX	AtomDB	CHIANTI	AS-RM	AS-REL
Mg XI	1s 4p $^1P_1$	1659.1	1659.1 (−0.0)	1659.1 (−0.0)	1660.2	1659.3
Mg XI	1s 5p $^1P_1$	1696.0	1696.0 (+0.0)	1696.0 (+0.0)	1697.1	1696.3
Al XII	1s 2p $^1P_1$	1598.3	1598.3 (−0.1)	1598.3 (−0.0)	1600.1	1599.1
Al XII	1s 2p $^3P_2$	1588.8	1588.8 (−0.0)	1588.8 (−0.0)	1589.9	1588.6
Al XII	1s 2p $^3P_1$	1588.2	1588.1 (−0.0)	1588.1 (−0.0)	1589.1	1588.0
Al XII	1s 2s $^3S_1$	1575.0	1575.0 (−0.1)	1575.0 (−0.0)	1576.0	1574.9
Al XII	1s 3p $^1P_1$	1868.8	1868.7 (−0.0)	1868.7 (−0.0)	1870.2	1869.0
Al XII	1s 4p $^1P_1$	1963.7	1963.7 (−0.0)	1963.7 (−0.0)	1965.1	1963.9
Al XII	1s 5p $^1P_1$	2007.7	2007.7 (−0.0)	2007.7 (−0.0)	2009.0	2007.9
Si XIII	1s 2p $^1P_1$	1865.0	1865.0 (−0.0)	1865.0 (+0.0)	1867.1	1865.8
Si XIII	1s 2p $^3P_2$	1854.6	1854.6 (+0.0)	1854.7 (+0.0)	1856.1	1854.5
Si XIII	1s 2p $^3P_1$	1853.8	1853.8 (−0.0)	1853.8 (+0.0)	1855.1	1853.6
Si XIII	1s 2s $^3S_1$	1839.4	1839.4 (−0.0)	1839.4 (+0.0)	1840.8	1839.4
Si XIII	1s 3p $^1P_1$	2182.5	2182.5 (−0.0)	2182.5 (−0.0)	2184.3	2182.9
Si XIII	1s 4p $^1P_1$	2294.0	2294.0 (+0.0)	2294.0 (+0.0)	2295.8	2294.3
Si XIII	1s 5p $^1P_1$	2345.7	2345.7 (+0.0)	2345.7 (+0.0)	2347.4	2346.0
P XIV	1s 2p $^1P_1$	2152.5	2152.4 (−0.1)	2152.4 (−0.1)	2154.9	2153.3
P XIV	1s 2p $^3P_2$	2141.4	2141.3 (−0.1)	2141.3 (−0.1)	2143.1	2141.1
P XIV	1s 2p $^3P_1$	2140.2	2140.1 (−0.1)	2140.1 (−0.1)	2141.7	2139.9
P XIV	1s 2s $^3S_1$	2124.7	2124.6 (−0.1)	2124.6 (−0.1)	2126.3	2124.5
P XIV	1s 3p $^1P_1$	2521.1	2521.0 (−0.1)	2521.0 (−0.1)	2523.1	2521.3
P XIV	1s 4p $^1P_1$	2650.4	2650.3 (−0.1)	2650.3 (−0.1)	2652.4	2650.6
P XIV	1s 5p $^1P_1$	2710.4	2710.3 (−0.1)	2710.2 (−0.1)	2712.3	2710.5
S XV	1s 2p $^1P_1$	2460.6	2460.6 (+0.0)	2460.6 (+0.0)	2463.5	2461.5
S XV	1s 2p $^3P_2$	2448.8	2448.8 (−0.0)	2448.8 (+0.0)	2450.9	2448.4
S XV	1s 2p $^3P_1$	2447.1	2447.1 (+0.0)	2447.0 (−0.1)	2449.1	2446.9
S XV	1s 2s $^3S_1$	2430.3	2430.3 (−0.0)	2430.4 (+0.0)	2432.5	2430.3
S XV	1s 3p $^1P_1$	2883.9	2883.9 (+0.0)	2883.9 (−0.0)	2886.5	2884.3
S XV	1s 4p $^1P_1$	3032.5	3032.5 (+0.0)	3032.5 (+0.0)	3035.0	3032.8
S XV	1s 5p $^1P_1$	3101.3	3101.3 (+0.0)	3101.3 (−0.0)	3103.8	3101.6
Cl XVI	1s 2p $^1P_1$	2789.8	2789.7 (−0.1)	2789.7 (−0.1)	2793.0	2790.6
Cl XVI	1s 2p $^3P_2$	2777.2	2777.1 (−0.1)	2777.1 (−0.1)	2779.7	2776.7
Cl XVI	1s 2p $^3P_1$	2775.1	2775.0 (−0.1)	2775.0 (−0.1)	2777.3	2774.6
Cl XVI	1s 2s $^3S_1$	2757.0	2756.9 (−0.1)	2756.9 (−0.1)	2759.4	2756.8
Cl XVI	1s 3p $^1P_1$	3271.7	3271.6 (−0.1)	3271.6 (−0.1)	3274.5	3271.9
Cl XVI	1s 4p $^1P_1$	3440.8	3440.8 (−0.0)	3440.8 (−0.0)	3443.6	3440.9
Cl XVI	1s 5p $^1P_1$	3519.2	3519.1 (−0.1)	3519.1 (−0.1)	3521.9	3519.2
Ar XVII	1s 2p $^1P_1$	3139.8	3139.6 (−0.2)	3139.6 (−0.2)	3143.5	3140.6
Ar XVII	1s 2p $^3P_2$	3126.5	3126.3 (−0.2)	3126.3 (−0.2)	3129.4	3125.8
Ar XVII	1s 2p $^3P_1$	3123.7	3123.5 (−0.2)	3123.5 (−0.2)	3126.4	3123.2
Ar XVII	1s 2s $^3S_1$	3104.3	3104.1 (−0.2)	3104.1 (−0.2)	3107.2	3104.1
Ar XVII	1s 3p $^1P_1$	3684.0	3683.8 (−0.2)	3684.0 (−0.0)	3687.4	3684.2
Ar XVII	1s 4p $^1P_1$	3875.0	3874.9 (−0.2)	3875.0 (−0.0)	3878.3	3875.1
Ar XVII	1s 5p $^1P_1$	3963.5	3963.3 (−0.2)	3963.5 (−0.0)	3966.8	3963.5
K XVIII	1s 2p $^1P_1$	3510.4	3510.5 (+0.2)	3510.4 (−0.0)	3515.0	3511.5
K XVIII	1s 2p $^3P_2$	3496.5	3496.5 (+0.1)	3496.5 (−0.0)	3500.2	3496.0
K XVIII	1s 2p $^3P_1$	3493.0	3493.0 (+0.1)	3493.0 (−0.0)	3496.4	3492.5
K XVIII	1s 2s $^3S_1$	3472.2	3472.3 (+0.1)	3472.2 (−0.0)	3475.9	3472.2
K XVIII	1s 3p $^1P_1$	4120.9	4120.8 (−0.1)	4120.9 (−0.0)	4125.1	4121.3
K XVIII	1s 4p $^1P_1$	4335.1	4335.1 (+0.0)	4335.1 (−0.0)	4339.2	4335.4
K XVIII	1s 5p $^1P_1$	4434.3	4434.3 (−0.0)	4434.3 (−0.0)	4438.4	4434.6
Ca XIX	1s 2p $^1P_1$	3902.3	3902.3 (−0.0)	3902.2 (−0.1)	3907.6	3903.5
Ca XIX	1s 2p $^3P_2$	3887.7	3887.7 (−0.0)	3887.6 (−0.1)	3892.2	3887.2
Ca XIX	1s 2p $^3P_1$	3883.3	3883.3 (−0.0)	3883.2 (−0.1)	3887.4	3882.8
Ca XIX	1s 2s $^3S_1$	3861.1	3861.1 (−0.0)	3861.1 (−0.0)	3865.6	3861.2
Ca XIX	1s 3p $^1P_1$	4582.8	4582.8 (−0.0)	4582.8 (−0.0)	4587.7	4583.3
Ca XIX	1s 4p $^1P_1$	4821.6	4821.6 (−0.0)	4821.6 (−0.0)	4826.4	4821.9
Ca XIX	1s 5p $^1P_1$	4932.2	4932.2 (−0.0)	4932.2 (−0.0)	4937.0	4932.5
Cr XXIII	1s 2p $^1P_1$	5682.1	5682.1 (+0.0)	5682.1 (+0.1)	5690.7	5683.6
Cr XXIII	1s 2p $^3P_2$	5665.1	5665.1 (−0.0)	5665.1 (+0.0)	5672.9	5664.1
Cr XXIII	1s 2p $^3P_1$	5654.8	5654.8 (−0.0)	5654.8 (−0.1)	5662.2	5654.1
Cr XXIII	1s 2s $^3S_1$	5626.9	5626.9 (+0.0)	5626.9 (+0.0)	5634.7	5627.0
Cr XXIII	1s 3p $^1P_1$	6680.8	6680.8 (−0.0)	6681.2 (+0.4)	6689.0	6681.4
Cr XXIII	1s 4p $^1P_1$	7031.2	7031.2 (+0.0)	7031.4 (+0.2)	7039.4	7031.6
Cr XXIII	1s 5p $^1P_1$	7193.4	7193.5 (+0.1)	7193.6 (+0.2)	7201.7	7193.8
Mn XXIV	1s 2p $^1P_1$	6180.2	6180.4 (+0.3)	⋯	6190.1	6182.1
Mn XXIV	1s 2p $^3P_2$	6162.8	6162.9 (+0.1)	⋯	6171.7	6161.8
Mn XXIV	1s 2p $^3P_1$	6150.7	6150.6 (−0.1)	⋯	6158.9	6149.8
Mn XXIV	1s 2s $^3S_1$	6121.1	6121.1 (+0.1)	⋯	6130.0	6121.3
Mn XXIV	1s 3p $^1P_1$	7268.2	7268.3 (+0.0)	⋯	7277.6	7268.9
Mn XXIV	1s 4p $^1P_1$	7649.9	7650.0 (+0.1)	⋯	7659.2	7650.4
Mn XXIV	1s 5p $^1P_1$	7826.6	7826.7 (+0.1)	⋯	7836.0	7827.0

Table 5
(Continued)

Ion	Level	SPEX	AtomDB	CHIANTI	AS-RM	AS-REL
Fe XXV	1s 2p $^1P_1$	6700.4	6700.4 (−0.0)	6700.5 (+0.1)	6711.2	6702.3
Fe XXV	1s 2p $^3P_2$	6682.3	6682.3 (+0.0)	6682.7 (+0.4)	6692.3	6681.1
Fe XXV	1s 2p $^3P_1$	6667.6	6667.6 (−0.0)	6667.7 (+0.1)	6677.0	6666.7
Fe XXV	1s 2s $^3S_1$	6636.6	6636.6 (+0.0)	6636.6 (+0.0)	6646.6	6636.8
Fe XXV	1s 3p $^1P_1$	7881.1	7881.2 (+0.0)	7881.1 (−0.0)	7891.6	7881.8
Fe XXV	1s 4p $^1P_1$	8295.4	8295.5 (+0.1)	8295.4 (−0.0)	8305.9	8295.9
Fe XXV	1s 5p $^1P_1$	8487.2	8487.3 (+0.1)	8487.2 (−0.0)	8497.7	8487.7
Ni XXVII	1s 2p $^1P_1$	7805.1	7805.6 (+0.4)	7805.6 (+0.5)	7818.9	7807.7
Ni XXVII	1s 2p $^3P_2$	7786.4	7786.4 (+0.0)	7786.4 (+0.1)	7798.9	7785.0
Ni XXVII	1s 2p $^3P_1$	7766.0	7765.7 (−0.4)	7765.7 (−0.3)	7777.7	7764.7
Ni XXVII	1s 2s $^3S_1$	7731.5	7731.6 (+0.1)	7731.6 (+0.1)	7744.2	7732.0
Ni XXVII	1s 3p $^1P_1$	9183.6	9183.6 (+0.0)	9183.6 (−0.0)	9196.6	9184.5
Ni XXVII	1s 4p $^1P_1$	9667.1	9667.2 (+0.1)	9667.1 (−0.0)	9680.2	9667.8
Ni XXVII	1s 5p $^1P_1$	9891.0	9891.1 (+0.1)	9891.0 (−0.0)	9904.1	9891.6

Note. The numbers in the parentheses are the differences (in eV) with respect to SPEX of the other two databases. The penultimate column shows the results of the present AUTOSTRUCTURE calculations which were used for the *R*-matrix calculations (AS-RM). The last column shows the results of AUTOSTRUCTURE calculations including relativistic effects (AS-REL) that are necessarily omitted by AS-RM. See the discussion in Section 6 and the Appendix.

Table 6
Lyman Transition Data of H-like Ions in SPEX v3.06.01, AtomDB v3.0.9, CHIANTI Database v10.0.1, and the Present Work (AUTOSTRUCTURE)

Ion	ID	λ (Å)	SPEX	AtomDB	CHIANTI	Δ	AS-RM	AS-REL
C VI	Ly$\alpha_{1/2}$	33.740	8.12×10^{11}	8.12×10^{11}	8.12×10^{11}	0.1%	8.12×10^{11}	8.12×10^{11}
C VI	Ly$\alpha_{3/2}$	33.734	8.12×10^{11}	8.12×10^{11}	8.12×10^{11}	0.1%	8.12×10^{11}	8.12×10^{11}
C VI	Ly$\beta_{1/2}$	28.466	2.17×10^{11}	2.17×10^{11}	2.16×10^{11}	0.3%	2.16×10^{11}	2.17×10^{11}
C VI	Ly$\beta_{3/2}$	28.465	2.17×10^{11}	2.17×10^{11}	2.16×10^{11}	0.3%	2.16×10^{11}	2.17×10^{11}
C VI	Ly$\gamma_{1/2}$	26.990	8.84×10^{10}	8.83×10^{10}	8.77×10^{10}	0.8%	8.78×10^{10}	8.82×10^{10}
C VI	Ly$\gamma_{3/2}$	26.990	8.84×10^{10}	8.84×10^{10}	8.79×10^{10}	0.5%	8.80×10^{10}	8.85×10^{10}
C VI	Ly$\delta_{1/2}$	26.357	4.46×10^{10}	4.45×10^{10}	4.38×10^{10}	1.7%	4.41×10^{10}	4.45×10^{10}
C VI	Ly$\delta_{3/2}$	26.357	4.46×10^{10}	4.46×10^{10}	4.40×10^{10}	1.4%	4.42×10^{10}	4.46×10^{10}
N VII	Ly$\alpha_{1/2}$	24.785	1.50×10^{12}	1.50×10^{12}	1.50×10^{12}	0.1%	1.50×10^{12}	1.50×10^{12}
N VII	Ly$\alpha_{3/2}$	24.779	1.51×10^{12}	1.50×10^{12}	1.51×10^{12}	0.2%	1.50×10^{12}	1.50×10^{12}
N VII	Ly$\beta_{1/2}$	20.911	4.02×10^{11}	4.01×10^{11}	4.02×10^{11}	0.2%	4.00×10^{11}	4.01×10^{11}
N VII	Ly$\beta_{3/2}$	20.910	4.02×10^{11}	4.02×10^{11}	4.02×10^{11}	0.2%	4.01×10^{11}	4.02×10^{11}
N VII	Ly$\gamma_{1/2}$	19.826	1.64×10^{11}	1.64×10^{11}	1.64×10^{11}	0.2%	1.62×10^{11}	1.63×10^{11}
N VII	Ly$\gamma_{3/2}$	19.826	1.64×10^{11}	1.64×10^{11}	1.64×10^{11}	0.2%	1.63×10^{11}	1.64×10^{11}
N VII	Ly$\delta_{1/2}$	19.361	8.26×10^{10}	8.24×10^{10}	8.26×10^{10}	0.2%	8.13×10^{10}	8.23×10^{10}
N VII	Ly$\delta_{3/2}$	19.361	8.26×10^{10}	8.26×10^{10}	8.27×10^{10}	0.2%	8.16×10^{10}	8.27×10^{10}
O VIII	Ly$\alpha_{1/2}$	18.973	2.57×10^{12}	2.57×10^{12}	2.56×10^{12}	0.1%	2.57×10^{12}	2.57×10^{12}
O VIII	Ly$\alpha_{3/2}$	18.967	2.57×10^{12}	2.57×10^{12}	2.56×10^{12}	0.2%	2.56×10^{12}	2.57×10^{12}
O VIII	Ly$\beta_{1/2}$	16.007	6.85×10^{11}	6.84×10^{11}	6.81×10^{11}	0.7%	6.81×10^{11}	6.84×10^{11}
O VIII	Ly$\beta_{3/2}$	16.006	6.86×10^{11}	6.86×10^{11}	6.83×10^{11}	0.5%	6.83×10^{11}	6.86×10^{11}
O VIII	Ly$\gamma_{1/2}$	15.176	2.80×10^{11}	2.79×10^{11}	2.76×10^{11}	1.4%	2.76×10^{11}	2.78×10^{11}
O VIII	Ly$\gamma_{3/2}$	15.176	2.79×10^{11}	2.80×10^{11}	2.77×10^{11}	1.0%	2.77×10^{11}	2.80×10^{11}
O VIII	Ly$\delta_{1/2}$	14.821	1.41×10^{11}	1.40×10^{11}	1.36×10^{11}	3.1%	1.38×10^{11}	1.40×10^{11}
O VIII	Ly$\delta_{3/2}$	14.820	1.41×10^{11}	1.41×10^{11}	1.38×10^{11}	2.5%	1.39×10^{11}	1.41×10^{11}
Ne X	Ly$\alpha_{1/2}$	12.138	6.27×10^{12}	6.26×10^{12}	6.26×10^{12}	0.2%	6.26×10^{12}	6.27×10^{12}
Ne X	Ly$\alpha_{3/2}$	12.133	6.28×10^{12}	6.27×10^{12}	6.26×10^{12}	0.3%	6.26×10^{12}	6.27×10^{12}
Ne X	Ly$\beta_{1/2}$	10.240	1.68×10^{12}	1.67×10^{12}	1.66×10^{12}	1.0%	1.66×10^{12}	1.67×10^{12}
Ne X	Ly$\beta_{3/2}$	10.239	1.68×10^{12}	1.68×10^{12}	1.66×10^{12}	0.7%	1.66×10^{12}	1.68×10^{12}
Ne X	Ly$\gamma_{1/2}$	9.709	6.83×10^{11}	6.80×10^{11}	6.70×10^{11}	2.0%	6.70×10^{11}	6.79×10^{11}
Ne X	Ly$\gamma_{3/2}$	9.709	6.83×10^{11}	6.83×10^{11}	6.74×10^{11}	1.3%	6.74×10^{11}	6.83×10^{11}
Ne X	Ly$\delta_{1/2}$	9.481	3.44×10^{11}	3.43×10^{11}	3.33×10^{11}	3.4%	3.33×10^{11}	3.41×10^{11}
Ne X	Ly$\delta_{3/2}$	9.481	3.44×10^{11}	3.44×10^{11}	3.36×10^{11}	2.4%	3.36×10^{11}	3.45×10^{11}
Na XI	Ly$\alpha_{1/2}$	10.029	9.19×10^{12}	9.17×10^{12}	9.19×10^{12}	0.2%	9.16×10^{12}	9.17×10^{12}
Na XI	Ly$\alpha_{3/2}$	10.023	9.20×10^{12}	9.18×10^{12}	9.22×10^{12}	0.4%	9.16×10^{12}	9.17×10^{12}
Na XI	Ly$\beta_{1/2}$	8.460	2.45×10^{12}	2.44×10^{12}	2.46×10^{12}	0.5%	2.42×10^{12}	2.44×10^{12}
Na XI	Ly$\beta_{3/2}$	8.459	2.45×10^{12}	2.45×10^{12}	2.46×10^{12}	0.2%	2.43×10^{12}	2.45×10^{12}
Na XI	Ly$\gamma_{1/2}$	8.021	1.00×10^{12}	9.95×10^{11}	1.00×10^{12}	0.6%	9.76×10^{11}	9.92×10^{11}
Na XI	Ly$\gamma_{3/2}$	8.021	1.00×10^{12}	1.00×10^{12}	1.00×10^{12}	0.2%	9.85×10^{11}	1.00×10^{12}
Na XI	Ly$\delta_{1/2}$	7.833	5.05×10^{11}	5.01×10^{11}	5.05×10^{11}	0.7%	4.84×10^{11}	4.99×10^{11}

Table 6
(Continued)

Ion	ID	λ (Å)	SPEX	AtomDB	CHIANTI	Δ	AS-RM	AS-REL
Na XI	Ly$\delta_{3/2}$	7.833	5.04×10^{11}	5.04×10^{11}	5.06×10^{11}	0.2%	4.89×10^{11}	5.05×10^{11}
Mg XII	Ly$\alpha_{1/2}$	8.425	1.30×10^{13}	1.30×10^{13}	1.30×10^{13}	0.3%	1.30×10^{13}	1.30×10^{13}
Mg XII	Ly$\alpha_{3/2}$	8.419	1.30×10^{13}	1.30×10^{13}	1.31×10^{13}	0.4%	1.30×10^{13}	1.30×10^{13}
MgXII	Ly$\beta_{1/2}$	7.107	3.48×10^{12}	3.46×10^{12}	3.48×10^{12}	0.6%	3.42×10^{12}	3.45×10^{12}
Mg XII	Ly$\beta_{3/2}$	7.106	3.48×10^{12}	3.48×10^{12}	3.48×10^{12}	0.2%	3.44×10^{12}	3.48×10^{12}
Mg XII	Ly$\gamma_{1/2}$	6.738	1.42×10^{12}	1.41×10^{12}	1.42×10^{12}	0.7%	1.38×10^{12}	1.40×10^{12}
Mg XII	Ly$\gamma_{3/2}$	6.738	1.42×10^{12}	1.42×10^{12}	1.42×10^{12}	0.2%	1.39×10^{12}	1.42×10^{12}
Mg XII	Ly$\delta_{1/2}$	6.580	7.15×10^{11}	7.09×10^{11}	7.15×10^{11}	0.8%	6.80×10^{11}	7.06×10^{11}
Mg XII	Ly$\delta_{3/2}$	6.580	7.15×10^{11}	7.15×10^{11}	7.16×10^{11}	0.2%	6.90×10^{11}	7.16×10^{11}
Al XIII	Ly$\alpha_{1/2}$	7.176	1.79×10^{13}	1.79×10^{13}	1.80×10^{13}	0.3%	1.79×10^{13}	1.79×10^{13}
Al XIII	Ly$\alpha_{3/2}$	7.171	1.80×10^{13}	1.79×10^{13}	1.80×10^{13}	0.5%	1.79×10^{13}	1.79×10^{13}
Al XIII	Ly$\beta_{1/2}$	6.054	4.79×10^{12}	4.76×10^{12}	4.80×10^{12}	0.7%	4.70×10^{12}	4.75×10^{12}
Al XIII	Ly$\beta_{3/2}$	6.053	4.80×10^{12}	4.79×10^{12}	4.80×10^{12}	0.3%	4.74×10^{12}	4.79×10^{12}
Al XIII	Ly$\gamma_{1/2}$	5.740	1.95×10^{12}	1.94×10^{12}	1.96×10^{12}	0.9%	1.89×10^{12}	1.93×10^{12}
Al XIII	Ly$\gamma_{3/2}$	5.739	1.95×10^{12}	1.95×10^{12}	1.96×10^{12}	0.2%	1.91×10^{12}	1.95×10^{12}
Al XIII	Ly$\delta_{1/2}$	5.605	9.85×10^{11}	9.76×10^{11}	9.86×10^{11}	1.0%	9.28×10^{11}	9.70×10^{11}
Al XIII	Ly$\delta_{3/2}$	5.605	9.85×10^{11}	9.85×10^{11}	9.87×10^{11}	0.2%	9.44×10^{11}	9.87×10^{11}
Si XIV	Ly$\alpha_{1/2}$	6.186	2.41×10^{13}	2.41×10^{13}	2.42×10^{13}	0.4%	2.40×10^{13}	2.41×10^{13}
Si XIV	Ly$\alpha_{3/2}$	6.180	2.42×10^{13}	2.41×10^{13}	2.42×10^{13}	0.5%	2.40×10^{13}	2.41×10^{13}
Si XIV	Ly$\beta_{1/2}$	5.218	6.45×10^{12}	6.40×10^{12}	6.45×10^{12}	0.9%	6.31×10^{12}	6.39×10^{12}
Si XIV	Ly$\beta_{3/2}$	5.217	6.45×10^{12}	6.45×10^{12}	6.47×10^{12}	0.3%	6.36×10^{12}	6.44×10^{12}
Si XIV	Ly$\gamma_{1/2}$	4.947	2.63×10^{12}	2.60×10^{12}	2.63×10^{12}	1.0%	2.53×10^{12}	2.59×10^{12}
Si XIV	Ly$\gamma_{3/2}$	4.947	2.63×10^{12}	2.63×10^{12}	2.64×10^{12}	0.3%	2.56×10^{12}	2.63×10^{12}
Si XIV	Ly$\delta_{1/2}$	4.831	1.33×10^{12}	1.31×10^{12}	1.33×10^{12}	1.1%	1.24×10^{12}	1.30×10^{12}
Si XIV	Ly$\delta_{3/2}$	4.831	1.33×10^{12}	1.32×10^{12}	1.33×10^{12}	0.3%	1.26×10^{12}	1.33×10^{12}
P XV	Ly$\alpha_{1/2}$	5.387	3.18×10^{13}	3.17×10^{13}	3.19×10^{13}	0.5%	3.16×10^{13}	3.17×10^{13}
P XV	Ly$\alpha_{3/2}$	5.381	3.19×10^{13}	3.18×10^{13}	3.20×10^{13}	0.6%	3.16×10^{13}	3.17×10^{13}
P XV	Ly$\beta_{1/2}$	4.544	8.51×10^{12}	8.43×10^{12}	8.51×10^{12}	1.0%	8.29×10^{12}	8.41×10^{12}
P XV	Ly$\beta_{3/2}$	4.543	8.51×10^{12}	8.50×10^{12}	8.53×10^{12}	0.3%	8.37×10^{12}	8.49×10^{12}
P XV	Ly$\gamma_{1/2}$	4.308	3.47×10^{12}	3.43×10^{12}	3.47×10^{12}	1.2%	3.31×10^{12}	3.41×10^{12}
P XV	Ly$\gamma_{3/2}$	4.308	3.47×10^{12}	3.47×10^{12}	3.48×10^{12}	0.3%	3.36×10^{12}	3.47×10^{12}
P XV	Ly$\delta_{1/2}$	4.207	1.75×10^{12}	1.73×10^{12}	1.75×10^{12}	1.3%	1.62×10^{12}	1.71×10^{12}
P XV	Ly$\delta_{3/2}$	4.207	1.75×10^{12}	1.75×10^{12}	1.75×10^{12}	0.3%	1.65×10^{12}	1.75×10^{12}
S XVI	Ly$\alpha_{1/2}$	4.733	4.12×10^{13}	4.10×10^{13}	4.13×10^{13}	0.6%	4.09×10^{13}	4.11×10^{13}
S XVI	Ly$\alpha_{3/2}$	4.727	4.14×10^{13}	4.12×10^{13}	4.14×10^{13}	0.7%	4.09×10^{13}	4.10×10^{13}
S XVI	Ly$\beta_{1/2}$	3.992	1.10×10^{13}	1.09×10^{13}	1.10×10^{13}	1.2%	1.07×10^{13}	1.09×10^{13}
S XVI	Ly$\beta_{3/2}$	3.991	1.10×10^{13}	1.10×10^{13}	1.10×10^{13}	0.4%	1.08×10^{13}	1.10×10^{13}
S XVI	Ly$\gamma_{1/2}$	3.785	4.49×10^{12}	4.44×10^{12}	4.50×10^{12}	1.4%	4.26×10^{12}	4.41×10^{12}
S XVI	Ly$\gamma_{3/2}$	3.784	4.49×10^{12}	4.49×10^{12}	4.50×10^{12}	0.3%	4.34×10^{12}	4.49×10^{12}
S XVI	Ly$\delta_{1/2}$	3.696	2.27×10^{12}	2.23×10^{12}	2.27×10^{12}	1.5%	2.07×10^{12}	2.21×10^{12}
S XVI	Ly$\delta_{3/2}$	3.696	2.27×10^{12}	2.26×10^{12}	2.27×10^{12}	0.4%	2.12×10^{12}	2.27×10^{12}
Cl XVII	Ly$\alpha_{1/2}$	4.191	5.26×10^{13}	5.23×10^{13}	5.26×10^{13}	0.7%	5.21×10^{13}	5.23×10^{13}
Cl XVII	Ly$\alpha_{3/2}$	4.185	5.28×10^{13}	5.25×10^{13}	5.29×10^{13}	0.7%	5.21×10^{13}	5.23×10^{13}
Cl XVII	Ly$\beta_{1/2}$	3.535	1.41×10^{13}	1.39×10^{13}	1.41×10^{13}	1.4%	1.36×10^{13}	1.38×10^{13}
Cl XVII	Ly$\beta_{3/2}$	3.534	1.41×10^{13}	1.40×10^{13}	1.41×10^{13}	0.4%	1.38×10^{13}	1.40×10^{13}
Cl XVII	Ly$\gamma_{1/2}$	3.351	5.73×10^{12}	5.65×10^{12}	5.74×10^{12}	1.6%	5.39×10^{12}	5.61×10^{12}
Cl XVII	Ly$\gamma_{3/2}$	3.351	5.73×10^{12}	5.72×10^{12}	5.74×10^{12}	0.3%	5.51×10^{12}	5.73×10^{12}
Cl XVII	Ly$\delta_{1/2}$	3.273	2.89×10^{12}	2.84×10^{12}	2.89×10^{12}	1.7%	2.61×10^{12}	2.81×10^{12}
Cl XVII	Ly$\delta_{3/2}$	3.272	2.89×10^{12}	2.89×10^{12}	2.90×10^{12}	0.4%	2.68×10^{12}	2.89×10^{12}
Ar XVIII	Ly$\alpha_{1/2}$	3.736	6.62×10^{13}	6.57×10^{13}	6.59×10^{13}	0.7%	6.55×10^{13}	6.58×10^{13}
Ar XVIII	Ly$\alpha_{3/2}$	3.731	6.64×10^{13}	6.60×10^{13}	6.55×10^{13}	1.3%	6.55×10^{13}	6.57×10^{13}
Ar XVIII	Ly$\beta_{1/2}$	3.151	1.77×10^{13}	1.74×10^{13}	1.75×10^{13}	1.4%	1.70×10^{13}	1.74×10^{13}
Ar XVIII	Ly$\beta_{3/2}$	3.150	1.77×10^{13}	1.76×10^{13}	1.75×10^{13}	1.0%	1.73×10^{13}	1.76×10^{13}
Ar XVIII	Ly$\gamma_{1/2}$	2.988	7.21×10^{12}	7.09×10^{12}	7.13×10^{12}	1.7%	6.73×10^{12}	7.04×10^{12}
Ar XVIII	Ly$\gamma_{3/2}$	2.987	7.21×10^{12}	7.20×10^{12}	7.16×10^{12}	0.7%	6.89×10^{12}	7.20×10^{12}
Ar XVIII	Ly$\delta_{1/2}$	2.918	3.64×10^{12}	3.57×10^{12}	3.59×10^{12}	1.9%	3.24×10^{12}	3.53×10^{12}
Ar XVIII	Ly$\delta_{3/2}$	2.917	3.64×10^{12}	3.63×10^{12}	3.60×10^{12}	0.9%	3.34×10^{12}	3.64×10^{12}
K XIX	Ly$\alpha_{1/2}$	3.352	8.22×10^{13}	8.16×10^{13}	8.23×10^{13}	0.8%	8.12×10^{13}	8.16×10^{13}
K XIX	Ly$\alpha_{3/2}$	3.347	8.25×10^{13}	8.19×10^{13}	8.27×10^{13}	0.9%	8.12×10^{13}	8.16×10^{13}
K XIX	Ly$\beta_{1/2}$	2.827	2.20×10^{13}	2.16×10^{13}	2.20×10^{13}	1.6%	2.11×10^{13}	2.16×10^{13}
K XIX	Ly$\beta_{3/2}$	2.826	2.20×10^{13}	2.19×10^{13}	2.20×10^{13}	0.5%	2.14×10^{13}	2.19×10^{13}
K XIX	Ly$\gamma_{1/2}$	2.680	8.96×10^{12}	8.79×10^{12}	8.96×10^{12}	2.0%	8.30×10^{12}	8.72×10^{12}
K XIX	Ly$\gamma_{3/2}$	2.680	8.96×10^{12}	8.94×10^{12}	8.98×10^{12}	0.4%	8.52×10^{12}	8.95×10^{12}
K XIX	Ly$\delta_{1/2}$	2.617	4.52×10^{12}	4.42×10^{12}	4.52×10^{12}	2.1%	3.97×10^{12}	4.37×10^{12}

Table 6
(Continued)

Ion	ID	λ (Å)	SPEX	AtomDB	CHIANTI	Δ	AS-RM	AS-REL
K XIX	Ly$\delta_{3/2}$	2.617	4.52×10^{12}	4.51×10^{12}	4.53×10^{12}	0.4%	4.11×10^{12}	4.52×10^{12}
Ca XX	Ly$\alpha_{1/2}$	3.024	1.01×10^{14}	1.00×10^{14}	1.01×10^{14}	1.0%	9.97×10^{13}	1.00×10^{14}
Ca XX	Ly$\alpha_{3/2}$	3.018	1.01×10^{14}	1.01×10^{14}	1.02×10^{14}	1.0%	9.97×10^{13}	1.00×10^{14}
Ca XX	Ly$\beta_{1/2}$	2.550	2.70×10^{13}	2.65×10^{13}	2.70×10^{13}	1.8%	2.58×10^{13}	2.64×10^{13}
Ca XX	Ly$\beta_{3/2}$	2.549	2.70×10^{13}	2.69×10^{13}	2.71×10^{13}	0.6%	2.62×10^{13}	2.69×10^{13}
Ca XX	Ly$\gamma_{1/2}$	2.418	1.10×10^{13}	1.08×10^{13}	1.10×10^{13}	2.2%	1.01×10^{13}	1.07×10^{13}
Ca XX	Ly$\gamma_{3/2}$	2.417	1.10×10^{13}	1.10×10^{13}	1.10×10^{13}	0.5%	1.04×10^{13}	1.10×10^{13}
Ca XX	Ly$\delta_{1/2}$	2.361	5.55×10^{12}	5.42×10^{12}	5.56×10^{12}	2.4%	4.80×10^{12}	5.35×10^{12}
Ca XX	Ly$\delta_{3/2}$	2.361	5.55×10^{12}	5.54×10^{12}	5.56×10^{12}	0.4%	5.00×10^{12}	5.56×10^{12}
Cr XXIV	Ly$\alpha_{1/2}$	2.096	2.10×10^{14}	2.08×10^{14}	⋯	1.3%	2.06×10^{14}	2.08×10^{14}
Cr XXIV	Ly$\alpha_{3/2}$	2.090	2.12×10^{14}	2.09×10^{14}	⋯	1.2%	2.06×10^{14}	2.08×10^{14}
Cr XXIV	Ly$\beta_{1/2}$	1.767	5.63×10^{13}	5.48×10^{13}	⋯	2.6%	5.25×10^{13}	5.45×10^{13}
Cr XXIV	Ly$\beta_{3/2}$	1.766	5.63×10^{13}	5.60×10^{13}	⋯	0.6%	5.38×10^{13}	5.59×10^{13}
Cr XXIV	Ly$\gamma_{1/2}$	1.675	2.29×10^{13}	2.22×10^{13}	⋯	3.1%	2.02×10^{13}	2.20×10^{13}
Cr XXIV	Ly$\gamma_{3/2}$	1.675	2.30×10^{13}	2.29×10^{13}	⋯	0.4%	2.11×10^{13}	2.29×10^{13}
Cr XXIV	Ly$\delta_{1/2}$	1.636	1.16×10^{13}	1.12×10^{13}	⋯	3.5%	9.35×10^{12}	1.10×10^{13}
Cr XXIV	Ly$\delta_{3/2}$	1.635	1.16×10^{13}	1.15×10^{13}	⋯	0.4%	9.92×10^{12}	1.16×10^{13}
Mn XXV	Ly$\alpha_{1/2}$	1.930	2.48×10^{14}	2.44×10^{14}	⋯	1.5%	2.42×10^{14}	2.45×10^{14}
Mn XXV	Ly$\alpha_{3/2}$	1.925	2.49×10^{14}	2.46×10^{14}	⋯	1.3%	2.42×10^{14}	2.44×10^{14}
Mn XXV	Ly$\beta_{1/2}$	1.627	6.63×10^{13}	6.44×10^{13}	⋯	2.8%	6.15×10^{13}	6.41×10^{13}
Mn XXV	Ly$\beta_{3/2}$	1.626	6.64×10^{13}	6.60×10^{13}	⋯	0.6%	6.32×10^{13}	6.58×10^{13}
Mn XXV	Ly$\gamma_{1/2}$	1.543	2.71×10^{13}	2.61×10^{13}	⋯	3.4%	2.36×10^{13}	2.58×10^{13}
Mn XXV	Ly$\gamma_{3/2}$	1.542	2.71×10^{13}	2.69×10^{13}	⋯	0.4%	2.47×10^{13}	2.70×10^{13}
Mn XXV	Ly$\delta_{1/2}$	1.506	1.36×10^{13}	1.31×10^{13}	⋯	3.7%	1.08×10^{13}	1.28×10^{13}
Mn XXV	Ly$\delta_{3/2}$	1.506	1.36×10^{13}	1.36×10^{13}	⋯	0.5%	1.15×10^{13}	1.37×10^{13}
Fe XXVI	Ly$\alpha_{1/2}$	1.784	2.90×10^{14}	2.86×10^{14}	2.91×10^{14}	1.7%	2.83×10^{14}	2.86×10^{14}
Fe XXVI	Ly$\alpha_{3/2}$	1.778	2.92×10^{14}	2.88×10^{14}	2.93×10^{14}	1.6%	2.83×10^{14}	2.86×10^{14}
Fe XXVI	Ly$\beta_{1/2}$	1.504	7.77×10^{13}	7.53×10^{13}	7.77×10^{13}	3.1%	7.15×10^{13}	7.49×10^{13}
Fe XXVI	Ly$\beta_{3/2}$	1.502	7.78×10^{13}	7.73×10^{13}	7.80×10^{13}	0.8%	7.37×10^{13}	7.71×10^{13}
Fe XXVI	Ly$\gamma_{1/2}$	1.425	3.17×10^{13}	3.05×10^{13}	3.17×10^{13}	3.7%	2.73×10^{13}	3.01×10^{13}
Fe XXVI	Ly$\gamma_{3/2}$	1.425	3.17×10^{13}	3.15×10^{13}	3.18×10^{13}	0.7%	2.87×10^{13}	3.16×10^{13}
Fe XXVI	Ly$\delta_{1/2}$	1.392	1.60×10^{13}	1.53×10^{13}	1.60×10^{13}	4.1%	1.24×10^{13}	1.50×10^{13}
Fe XXVI	Ly$\delta_{3/2}$	1.392	1.60×10^{13}	1.59×10^{13}	1.60×10^{13}	0.7%	1.33×10^{13}	1.60×10^{13}
Ni XXVIII	Ly$\alpha_{1/2}$	1.536	3.92×10^{14}	3.84×10^{14}	3.92×10^{14}	2.0%	3.80×10^{14}	3.85×10^{14}
Ni XXVIII	Ly$\alpha_{3/2}$	1.530	3.95×10^{14}	3.88×10^{14}	3.95×10^{14}	1.9%	3.80×10^{14}	3.84×10^{14}
Ni XXVIII	Ly$\beta_{1/2}$	1.294	1.05×10^{14}	1.01×10^{14}	1.05×10^{14}	3.7%	9.51×10^{13}	1.00×10^{14}
Ni XXVIII	Ly$\beta_{3/2}$	1.293	1.05×10^{14}	1.04×10^{14}	1.05×10^{14}	1.0%	9.85×10^{13}	1.04×10^{14}
Ni XXVIII	Ly$\gamma_{1/2}$	1.227	4.27×10^{13}	4.09×10^{13}	4.28×10^{13}	4.3%	3.59×10^{13}	4.02×10^{13}
Ni XXVIII	Ly$\gamma_{3/2}$	1.227	4.28×10^{13}	4.25×10^{13}	4.29×10^{13}	0.8%	3.81×10^{13}	4.26×10^{13}
Ni XXVIII	Ly$\delta_{1/2}$	1.198	2.16×10^{13}	2.05×10^{13}	2.16×10^{13}	4.7%	1.60×10^{13}	2.00×10^{13}
Ni XXVIII	Ly$\delta_{3/2}$	1.198	2.16×10^{13}	2.14×10^{13}	2.16×10^{13}	0.8%	1.74×10^{13}	2.16×10^{13}

Note. The wavelengths (as in SPEX) are in angstroms and A-values in s^{-1}. The column labeled Δ is the maximum percentage deviation ((max–min)/max $\times$ 100%) among the three databases. The penultimate column shows the results of the present AUTOSTRUCTURE calculations which were used for the R-matrix calculations (AS-RM). The last column shows the results of AUTOSTRUCTURE calculations including relativistic effects (AS-REL) that are necessarily omitted by AS-RM. See the discussion in Section 6 and the Appendix.

Table 7
Transition Data of He-like Ions in SPEX v3.06.01, AtomDB v3.0.9, and CHIANTI Database v10.0.1, and the Present Work (AUTOSTRUCTURE)

Ion	ID	λ (Å)	SPEX	AtomDB	CHIANTI	Δ	AS-RM	AS-REL
C V	Heα-z	41.472	4.96×10^{1}	4.05×10^{1}	4.05×10^{1}	18.3%	4.05×10^{1}	4.53×10^{1}
C V	Heα-y	40.731	2.89×10^{7}	1.76×10^{7}	2.24×10^{7}	39.1%	1.76×10^{7}	2.14×10^{7}
C V	Heα-x	40.728	2.65×10^{4}	2.49×10^{4}	2.54×10^{4}	6.0%	2.53×10^{4}	2.52×10^{4}
C V	Heα-w	40.268	8.87×10^{11}	9.34×10^{11}	9.23×10^{11}	5.0%	9.33×10^{11}	9.33×10^{11}
C V	Heβ-w	34.973	2.55×10^{11}	2.84×10^{11}	2.78×10^{11}	10.1%	2.82×10^{11}	2.83×10^{11}
C V	Heγ-w	33.426	1.07×10^{11}	1.25×10^{11}	1.21×10^{11}	14.8%	1.23×10^{11}	1.24×10^{11}
C V	Heδ-w	32.754	5.43×10^{10}	6.97×10^{10}	6.42×10^{10}	22.2%	6.60×10^{10}	6.66×10^{10}
N VI	Heα-z	29.534	2.57×10^{2}	2.17×10^{2}	2.17×10^{2}	15.6%	2.17×10^{2}	2.39×10^{2}
N VI	Heα-y	29.084	1.42×10^{8}	9.26×10^{7}	1.14×10^{8}	34.6%	9.27×10^{7}	1.09×10^{8}
N VI	Heα-x	29.081	1.04×10^{5}	9.88×10^{4}	1.00×10^{5}	4.6%	9.98×10^{4}	9.97×10^{4}

Table 7
(Continued)

Ion	ID	λ (Å)	SPEX	AtomDB	CHIANTI	Δ	AS-RM	AS-REL
N VI	Heα-w	28.787	1.81×10^{12}	1.89×10^{12}	1.87×10^{12}	4.3%	1.89×10^{12}	1.89×10^{12}
N VI	Heβ-w	24.898	5.16×10^{11}	5.62×10^{11}	5.54×10^{11}	8.2%	5.60×10^{11}	5.61×10^{11}
N VI	Heγ-w	23.771	2.14×10^{11}	2.44×10^{11}	2.38×10^{11}	12.1%	2.41×10^{11}	2.43×10^{11}
N VI	Heδ-w	23.277	1.09×10^{11}	1.33×10^{11}	1.25×10^{11}	18.0%	1.28×10^{11}	1.29×10^{11}
O VII	Heα-z	22.101	1.06×10^{3}	9.12×10^{2}	9.12×10^{2}	14.0%	9.14×10^{2}	9.95×10^{2}
O VII	Heα-y	21.807	5.56×10^{8}	3.83×10^{8}	4.59×10^{8}	31.1%	3.84×10^{8}	4.43×10^{8}
O VII	Heα-x	21.804	3.33×10^{5}	3.20×10^{5}	3.24×10^{5}	3.9%	3.22×10^{5}	3.21×10^{5}
O VII	Heα-w	21.602	3.31×10^{12}	3.43×10^{12}	3.40×10^{12}	3.5%	3.43×10^{12}	3.43×10^{12}
O VII	Heβ-w	18.627	9.36×10^{11}	1.01×10^{12}	9.95×10^{11}	7.3%	1.00×10^{12}	1.01×10^{12}
O VII	Heγ-w	17.768	3.92×10^{11}	4.32×10^{11}	4.24×10^{11}	9.3%	4.28×10^{11}	4.31×10^{11}
O VII	Heδ-w	17.396	1.97×10^{11}	2.31×10^{11}	2.22×10^{11}	14.6%	2.24×10^{11}	2.28×10^{11}
Ne IX	Heα-z	13.699	1.10×10^{4}	9.77×10^{3}	9.77×10^{3}	11.2%	9.78×10^{3}	1.05×10^{4}
Ne IX	Heα-y	13.553	5.40×10^{9}	3.98×10^{9}	4.63×10^{9}	26.3%	3.98×10^{9}	4.45×10^{9}
Ne IX	Heα-x	13.550	2.27×10^{6}	2.20×10^{6}	2.22×10^{6}	2.9%	2.21×10^{6}	2.21×10^{6}
Ne IX	Heα-w	13.447	8.89×10^{12}	9.12×10^{12}	9.05×10^{12}	2.6%	9.12×10^{12}	9.12×10^{12}
Ne IX	Heβ-w	11.547	2.49×10^{12}	2.62×10^{12}	2.60×10^{12}	5.0%	2.61×10^{12}	2.63×10^{12}
Ne IX	Heγ-w	11.000	1.03×10^{12}	1.10×10^{12}	1.10×10^{12}	6.5%	1.10×10^{12}	1.11×10^{12}
Ne IX	Heδ-w	10.764	5.22×10^{11}	5.77×10^{11}	5.70×10^{11}	9.6%	5.67×10^{11}	5.83×10^{11}
Na X	Heα-z	11.191	2.97×10^{4}	2.66×10^{4}	2.75×10^{4}	10.4%	2.67×10^{4}	2.85×10^{4}
Na X	Heα-y	11.083	1.42×10^{10}	1.07×10^{10}	1.39×10^{10}	24.5%	1.07×10^{10}	1.18×10^{10}
Na X	Heα-x	11.080	5.08×10^{6}	4.98×10^{6}	5.03×10^{6}	2.1%	4.98×10^{6}	4.97×10^{6}
Na X	Heα-w	11.003	1.35×10^{13}	1.38×10^{13}	1.40×10^{13}	3.6%	1.38×10^{13}	1.38×10^{13}
Na X	Heβ-w	9.433	3.73×10^{12}	3.91×10^{12}	4.20×10^{12}	11.2%	3.91×10^{12}	3.94×10^{12}
Na X	Heγ-w	8.983	1.54×10^{12}	1.64×10^{12}	1.97×10^{12}	21.8%	1.63×10^{12}	1.66×10^{12}
Na X	Heδ-w	8.788	7.82×10^{11}	8.47×10^{11}	1.22×10^{12}	36.0%	8.39×10^{11}	8.67×10^{11}
Mg XI	Heα-z	9.314	7.33×10^{4}	6.63×10^{4}	6.63×10^{4}	9.5%	6.64×10^{4}	7.08×10^{4}
Mg XI	Heα-y	9.231	3.40×10^{10}	2.61×10^{10}	2.99×10^{10}	23.2%	2.61×10^{10}	2.85×10^{10}
Mg XI	Heα-x	9.228	1.06×10^{7}	1.04×10^{7}	1.04×10^{7}	1.9%	1.04×10^{7}	1.04×10^{7}
Mg XI	Heα-w	9.169	1.96×10^{13}	2.00×10^{13}	1.98×10^{13}	2.0%	2.00×10^{13}	2.00×10^{13}
Mg XI	Heβ-w	7.847	5.42×10^{12}	5.64×10^{12}	5.63×10^{12}	4.0%	5.63×10^{12}	5.68×10^{12}
Mg XI	Heγ-w	7.473	2.23×10^{12}	2.35×10^{12}	2.36×10^{12}	5.5%	2.35×10^{12}	2.39×10^{12}
Mg XI	Heδ-w	7.310	1.13×10^{12}	1.20×10^{12}	1.22×10^{12}	7.2%	1.20×10^{12}	1.24×10^{12}
Al XII	Heα-z	7.872	1.68×10^{5}	1.53×10^{5}	1.53×10^{5}	8.8%	1.53×10^{5}	1.63×10^{5}
Al XII	Heα-y	7.807	7.57×10^{10}	5.89×10^{10}	6.71×10^{10}	22.2%	5.89×10^{10}	6.38×10^{10}
Al XII	Heα-x	7.804	2.08×10^{7}	2.05×10^{7}	...	1.6%	2.05×10^{7}	2.04×10^{7}
Al XII	Heα-w	7.757	2.76×10^{13}	2.81×10^{13}	2.79×10^{13}	1.6%	2.80×10^{13}	2.81×10^{13}
Al XII	Heβ-w	6.635	7.63×10^{12}	7.87×10^{12}	7.88×10^{12}	3.2%	7.86×10^{12}	7.94×10^{12}
Al XII	Heγ-w	6.314	3.13×10^{12}	3.27×10^{12}	3.30×10^{12}	5.0%	3.26×10^{12}	3.34×10^{12}
Al XII	Heδ-w	6.175	1.59×10^{12}	1.65×10^{12}	1.70×10^{12}	6.4%	1.65×10^{12}	1.73×10^{12}
Si XIII	Heα-z	6.740	3.61×10^{5}	3.31×10^{5}	3.31×10^{5}	8.3%	3.31×10^{5}	3.51×10^{5}
Si XIII	Heα-y	6.688	1.58×10^{11}	1.24×10^{11}	1.41×10^{11}	21.5%	1.24×10^{11}	1.34×10^{11}
Si XIII	Heα-x	6.685	3.89×10^{7}	3.83×10^{7}	3.82×10^{7}	1.8%	3.82×10^{7}	3.81×10^{7}
Si XIII	Heα-w	6.648	3.76×10^{13}	3.84×10^{13}	3.82×10^{13}	2.0%	3.83×10^{13}	3.84×10^{13}
Si XIII	Heβ-w	5.681	1.04×10^{13}	1.07×10^{13}	1.07×10^{13}	2.8%	1.07×10^{13}	1.08×10^{13}
Si XIII	Heγ-w	5.405	4.29×10^{12}	4.42×10^{12}	4.48×10^{12}	4.2%	4.41×10^{12}	4.53×10^{12}
Si XIII	Heδ-w	5.286	2.17×10^{12}	2.21×10^{12}	2.30×10^{12}	5.5%	2.23×10^{12}	2.35×10^{12}
P XIV	Heα-z	5.835	7.35×10^{5}	6.76×10^{5}	7.34×10^{5}	8.1%	6.77×10^{5}	7.18×10^{5}
P XIV	Heα-y	5.793	3.12×10^{11}	2.48×10^{11}	3.12×10^{11}	20.6%	2.48×10^{11}	2.64×10^{11}
P XIV	Heα-x	5.790	6.94×10^{7}	6.82×10^{7}	6.94×10^{7}	1.7%	6.81×10^{7}	6.79×10^{7}
P XIV	Heα-w	5.760	5.03×10^{13}	5.12×10^{13}	5.01×10^{13}	2.2%	5.12×10^{13}	5.13×10^{13}
P XIV	Heβ-w	4.918	1.39×10^{13}	1.42×10^{13}	1.30×10^{13}	8.7%	1.42×10^{13}	1.44×10^{13}
P XIV	Heγ-w	4.678	5.72×10^{12}	5.84×10^{12}	5.20×10^{12}	11.0%	5.84×10^{12}	6.02×10^{12}
P XIV	Heδ-w	4.574	2.90×10^{12}	2.89×10^{12}	2.69×10^{12}	7.0%	2.93×10^{12}	3.11×10^{12}
S XV	Heα-z	5.101	1.43×10^{6}	1.32×10^{6}	1.32×10^{6}	7.7%	1.32×10^{6}	1.40×10^{6}
S XV	Heα-y	5.066	5.87×10^{11}	4.68×10^{11}	5.22×10^{11}	20.3%	4.68×10^{11}	4.96×10^{11}
S XV	Heα-x	5.063	1.19×10^{8}	1.17×10^{8}	1.17×10^{8}	1.7%	1.17×10^{8}	1.16×10^{8}
S XV	Heα-w	5.039	6.58×10^{13}	6.70×10^{13}	6.68×10^{13}	1.8%	6.70×10^{13}	6.72×10^{13}
S XV	Heβ-w	4.299	1.82×10^{13}	1.85×10^{13}	1.87×10^{13}	2.9%	1.85×10^{13}	1.88×10^{13}
S XV	Heγ-w	4.088	7.45×10^{12}	7.56×10^{12}	7.76×10^{12}	4.0%	7.57×10^{12}	7.85×10^{12}
S XV	Heδ-w	3.998	3.77×10^{12}	3.71×10^{12}	3.98×10^{12}	6.8%	3.78×10^{12}	4.05×10^{12}
Cl XVI	Heα-z	4.497	2.67×10^{6}	2.47×10^{6}	2.68×10^{6}	7.8%	2.47×10^{6}	2.62×10^{6}
Cl XVI	Heα-y	4.468	1.06×10^{12}	8.45×10^{11}	1.06×10^{12}	20.0%	8.46×10^{11}	8.89×10^{11}
Cl XVI	Heα-x	4.464	1.97×10^{8}	1.94×10^{8}	1.97×10^{8}	1.5%	1.93×10^{8}	1.93×10^{8}
Cl XVI	Heα-w	4.444	8.47×10^{13}	8.61×10^{13}	8.47×10^{13}	1.6%	8.61×10^{13}	8.64×10^{13}

Table 7
(Continued)

Ion	ID	λ (Å)	SPEX	AtomDB	CHIANTI	Δ	AS-RM	AS-REL
Cl XVI	Heβ-w	3.790	2.32×10^{13}	2.36×10^{13}	2.25×10^{13}	4.8%	2.36×10^{13}	2.41×10^{13}
Cl XVI	Heγ-w	3.603	9.45×10^{12}	9.62×10^{12}	9.09×10^{12}	5.5%	9.65×10^{12}	1.00×10^{13}
Cl XVI	Heδ-w	3.523	4.77×10^{12}	4.67×10^{12}	4.53×10^{12}	5.1%	4.79×10^{12}	5.18×10^{12}
Ar XVII	Heα-z	3.994	4.80×10^{6}	4.45×10^{6}	4.45×10^{6}	7.3%	4.45×10^{6}	4.72×10^{6}
Ar XVII	Heα-y	3.969	1.82×10^{12}	1.46×10^{12}	1.65×10^{12}	19.8%	1.46×10^{12}	1.53×10^{12}
Ar XVII	Heα-x	3.966	3.16×10^{8}	3.13×10^{8}	3.11×10^{8}	1.6%	3.11×10^{8}	3.10×10^{8}
Ar XVII	Heα-w	3.949	1.07×10^{14}	1.09×10^{14}	1.09×10^{14}	1.6%	1.09×10^{14}	1.09×10^{14}
Ar XVII	Heβ-w	3.365	2.91×10^{13}	2.98×10^{13}	⋯	2.3%	2.98×10^{13}	3.04×10^{13}
Ar XVII	Heγ-w	3.200	1.18×10^{13}	1.20×10^{13}	⋯	1.4%	1.21×10^{13}	1.27×10^{13}
Ar XVII	Heδ-w	3.128	5.96×10^{12}	5.78×10^{12}	⋯	3.1%	5.97×10^{12}	6.52×10^{12}
K XVIII	Heα-z	3.571	8.37×10^{6}	7.76×10^{6}	8.30×10^{6}	7.3%	7.77×10^{6}	8.24×10^{6}
K XVIII	Heα-y	3.550	3.02×10^{12}	2.44×10^{12}	3.02×10^{12}	19.3%	2.44×10^{12}	2.54×10^{12}
K XVIII	Heα-x	3.546	4.94×10^{8}	4.90×10^{8}	4.92×10^{8}	0.8%	4.87×10^{8}	4.85×10^{8}
K XVIII	Heα-w	3.532	1.34×10^{14}	1.36×10^{14}	1.35×10^{14}	1.7%	1.36×10^{14}	1.36×10^{14}
K XVIII	Heβ-w	3.009	3.60×10^{13}	3.69×10^{13}	3.54×10^{13}	4.0%	3.70×10^{13}	3.78×10^{13}
K XVIII	Heγ-w	2.860	1.46×10^{13}	1.49×10^{13}	1.43×10^{13}	4.0%	1.50×10^{13}	1.57×10^{13}
K XVIII	Heδ-w	2.796	7.37×10^{12}	7.06×10^{12}	7.20×10^{12}	4.2%	7.34×10^{12}	8.09×10^{12}
Ca XIX	Heα-z	3.211	1.42×10^{7}	1.31×10^{7}	1.36×10^{7}	7.7%	1.32×10^{7}	1.40×10^{7}
Ca XIX	Heα-y	3.193	4.84×10^{12}	3.93×10^{12}	4.42×10^{12}	18.8%	3.93×10^{12}	4.06×10^{12}
Ca XIX	Heα-x	3.189	7.55×10^{8}	7.51×10^{8}	7.45×10^{8}	1.3%	7.45×10^{8}	7.42×10^{8}
Ca XIX	Heα-w	3.177	1.64×10^{14}	1.67×10^{14}	1.67×10^{14}	1.6%	1.67×10^{14}	1.68×10^{14}
Ca XIX	Heβ-w	2.705	4.40×10^{13}	4.52×10^{13}	4.61×10^{13}	4.5%	4.53×10^{13}	4.64×10^{13}
Ca XIX	Heγ-w	2.571	1.79×10^{13}	1.81×10^{13}	1.91×10^{13}	6.3%	1.82×10^{13}	1.93×10^{13}
Ca XIX	Heδ-w	2.514	9.02×10^{12}	8.50×10^{12}	9.73×10^{12}	12.6%	8.90×10^{12}	9.91×10^{12}
Cr XXIII	Heα-z	2.203	9.17×10^{7}	8.52×10^{7}	8.52×10^{7}	7.1%	8.53×10^{7}	9.13×10^{7}
Cr XXIII	Heα-y	2.192	2.22×10^{13}	1.95×10^{13}	2.17×10^{13}	12.0%	1.95×10^{13}	1.98×10^{13}
Cr XXIII	Heα-x	2.189	3.39×10^{9}	3.40×10^{9}	3.35×10^{9}	1.4%	3.36×10^{9}	3.34×10^{9}
Cr XXIII	Heα-w	2.182	3.37×10^{14}	3.43×10^{14}	3.42×10^{14}	1.9%	3.44×10^{14}	3.46×10^{14}
Cr XXIII	Heβ-w	1.856	9.07×10^{13}	9.12×10^{13}	9.39×10^{13}	3.4%	9.14×10^{13}	9.49×10^{13}
Cr XXIII	Heγ-w	1.763	3.76×10^{13}	3.58×10^{13}	3.87×10^{13}	7.5%	3.62×10^{13}	3.93×10^{13}
Cr XXIII	Heδ-w	1.724	1.87×10^{13}	1.60×10^{13}	1.97×10^{13}	18.8%	1.72×10^{13}	2.02×10^{13}
Mn XXIV	Heα-z	2.026	1.39×10^{8}	1.29×10^{8}	⋯	7.3%	1.29×10^{8}	1.39×10^{8}
Mn XXIV	Heα-y	2.016	3.11×10^{13}	2.72×10^{13}	⋯	12.6%	2.72×10^{13}	2.76×10^{13}
Mn XXIV	Heα-x	2.012	4.75×10^{9}	4.76×10^{9}	⋯	0.2%	4.70×10^{9}	4.67×10^{9}
Mn XXIV	Heα-w	2.006	3.93×10^{14}	4.02×10^{14}	⋯	2.1%	4.02×10^{14}	4.05×10^{14}
Mn XXIV	Heβ-w	1.706	1.07×10^{14}	1.06×10^{14}	⋯	0.5%	1.06×10^{14}	1.11×10^{14}
Mn XXIV	Heγ-w	1.621	4.39×10^{13}	4.14×10^{13}	⋯	5.7%	4.20×10^{13}	4.59×10^{13}
Mn XXIV	Heδ-w	1.584	2.19×10^{13}	1.82×10^{13}	⋯	16.8%	1.98×10^{13}	2.35×10^{13}
Fe XXV	Heα-z	1.868	2.08×10^{8}	1.93×10^{8}	1.93×10^{8}	7.2%	1.93×10^{8}	2.08×10^{8}
Fe XXV	Heα-y	1.859	4.26×10^{13}	3.72×10^{13}	4.10×10^{13}	12.7%	3.72×10^{13}	3.76×10^{13}
Fe XXV	Heα-x	1.855	6.55×10^{9}	6.58×10^{9}	6.47×10^{9}	1.6%	6.49×10^{9}	6.44×10^{9}
Fe XXV	Heα-w	1.850	4.57×10^{14}	4.67×10^{14}	4.65×10^{14}	2.2%	4.67×10^{14}	4.71×10^{14}
Fe XXV	Heβ-w	1.573	1.24×10^{14}	1.23×10^{14}	1.27×10^{14}	3.1%	1.23×10^{14}	1.29×10^{14}
Fe XXV	Heγ-w	1.495	5.05×10^{13}	4.76×10^{13}	5.23×10^{13}	9.0%	4.84×10^{13}	5.33×10^{13}
Fe XXV	Heδ-w	1.461	2.54×10^{13}	2.06×10^{13}	2.66×10^{13}	22.6%	2.26×10^{13}	2.73×10^{13}
Ni XXVII	Heα-z	1.604	4.45×10^{8}	4.11×10^{8}	4.11×10^{8}	7.6%	4.12×10^{8}	4.46×10^{8}
Ni XXVII	Heα-y	1.597	7.49×10^{13}	6.53×10^{13}	7.15×10^{13}	12.8%	6.54×10^{13}	6.59×10^{13}
Ni XXVII	Heα-x	1.592	1.20×10^{10}	1.21×10^{10}	1.19×10^{10}	1.8%	1.19×10^{10}	1.18×10^{10}
Ni XXVII	Heα-w	1.589	6.02×10^{14}	6.17×10^{14}	6.15×10^{14}	2.5%	6.17×10^{14}	6.24×10^{14}
Ni XXVII	Heβ-w	1.350	1.63×10^{14}	1.61×10^{14}	1.68×10^{14}	4.2%	1.61×10^{14}	1.70×10^{14}
Ni XXVII	Heγ-w	1.282	6.38×10^{13}	6.17×10^{13}	6.89×10^{13}	10.4%	6.28×10^{13}	7.04×10^{13}
Ni XXVII	Heδ-w	1.254	3.35×10^{13}	2.59×10^{13}	3.49×10^{13}	25.8%	2.90×10^{13}	3.61×10^{13}

Note. The wavelengths (as in SPEX) are in units of angstroms and A-values in s^{-1}. The column labeled Δ is the maximum percentage deviation ((max–min)/max $\times$ 100%) among the three databases. The penultimate column shows the results of the present AUTOSTRUCTURE calculations which were used for the R-matrix calculations (AS-RM). The last column shows the results of AUTOSTRUCTURE calculations including relativistic effects (AS-REL) that are necessarily omitted by AS-RM. See the discussion in Section 6 and the Appendix.

ORCID iDs

Junjie Mao https://orcid.org/0000-0001-7557-9713
G. Del Zanna https://orcid.org/0000-0002-4125-0204
Liyi Gu https://orcid.org/0000-0001-9911-7038

References

Aggarwal, K. M., & Keenan, F. P. 2010, PhyS, 82, 065302
Aggarwal, K. M., & Keenan, F. P. 2012a, PhyS, 85, 025305
Aggarwal, K. M., & Keenan, F. P. 2012b, PhyS, 85, 025306
Aggarwal, K. M., & Keenan, F. P. 2013, PhyS, 87, 055302
Aggarwal, K. M., Keenan, F. P., & Heeter, R. F. 2009, PhyS, 80, 045301
Aggarwal, K. M., Keenan, F. P., & Heeter, R. F. 2010, PhyS, 82, 015006
Aggarwal, K. M., & Kingston, A. E. 1991a, JPhB, 24, 4583
Aggarwal, K. M., & Kingston, A. E. 1991b, PhyS, 44, 517
Aggarwal, K. M., & Kingston, A. E. 1992a, PhyS, 46, 193
Aggarwal, K. M., & Kingston, A. E. 1992b, JPhB, 25, 751
Anders, E., & Grevesse, N. 1989, GeCoA, 53, 197
Arnaud, K. A. 1996, in ASP Conf. Ser. 101, Astronomical Data Analysis Software and Systems V, ed. G. H. Jacoby & J. Barnes (San Francisco, CA: ASP), 17
Asplund, M., Grevesse, N., Sauval, A. J., & Scott, P. 2009, ARA&A, 47, 481
Badnell, N. R. 2006, ApJS, 167, 334
Badnell, N. R. 2011, CoPhC, 182, 1528
Badnell, N. R., & Griffin, D. C. 2001, JPhB, 34, 681
Ballance, C. P., Badnell, N. R., & Berrington, K. A. 2002, JPhB, 35, 1095
Ballance, C. P., Badnell, N. R., & Smyth, E. S. 2003, JPhB, 36, 3707
Barret, D., Lam Trong, T., den Herder, J.-W., et al. 2018, Proc. SPIE, 10699, 106991G
Betancourt-Martinez, G., Akamatsu, H., Barret, D., et al. 2019, BAAS, 51, 337
Betancourt-Martinez, G. L., Cumbee, R. S., & Leutenegger, M. A. 2020, AN, 341, 197
Branduardi-Raymont, G., Bhardwaj, A., Elsner, R. F., et al. 2007, A&A, 463, 761
Bryans, P., Landi, E., & Savin, D. W. 2009, ApJ, 691, 1540
Burgess, A. 1974, JPhB, 7, L364
Burgess, A., & Tully, J. A. 1992, A&A, 254, 436
Chakraborty, P, Ferland, G. J., Chatzikos, M., Guzmán, F., & Su, Y. 2021, ApJ, 912, 26
Chakraborty, P., Ferland, G. J., Chatzikos, M., et al. 2022, ApJ, 935, 70
Chen, Y., Wang, Q. D., Zhang, G.-Y., Zhang, S., & Ji, L. 2018, ApJ, 861, 138
Cui, W., Chen, L.-B., Gao, B., et al. 2020, JLTP, 199, 502
Del Zanna, G., Dere, K. P., Young, P. R., & Landi, E. 2021, ApJ, 909, 38
Del Zanna, G., Fernández-Menchero, L., & Badnell, N. R. 2019, MNRAS, 484, 4754
Del Zanna, G., & Mason, H. E. 2018, LRSP, 15, 5
Dere, K. P., Del Zanna, G., Young, P. R., Landi, E., & Sutherland, R. S. 2019, ApJS, 241, 22
Dere, K. P., Landi, E., Mason, H. E., Monsignori Fossi, B. C., & Young, P. R. 1997, A&AS, 125, 149
Dere, K. P., Landi, E., Young, P. R., et al. 2009, A&A, 498, 915
Dufresne, R. P., & Del Zanna, G. 2019, A&A, 626, A123
Dufresne, R. P., Del Zanna, G., & Badnell, N. R. 2020, MNRAS, 497, 1443
Dufresne, R. P., Del Zanna, G., & Storey, P. J. 2021, MNRAS, 505, 3968
Eissner, W., Jones, M., & Nussbaumer, H. 1974, CoPhC, 8, 270
Fernández-Menchero, L., Zatsarinny, O., & Bartschat, K. 2017, JPhB, 50, 065203
Foster, A. R., Ji, L., Smith, R. K., & Brickhouse, N. S. 2012, ApJ, 756, 128
Gorczyca, T. W., & Badnell, N. R. 1996, JPhB, 29, L283
Griffin, D. C., Badnell, N. R., & Pindzola, M. S. 1998, JPhB, 31, 3713
Gu, L., Kaastra, J., & Raassen, A. J. J. 2016, A&A, 588, A52
Gu, L., Raassen, A. J. J., Mao, J., et al. 2019, A&A, 627, A51
Gu, L., Shah, C., Mao, J., et al. 2020, A&A, 641, A93
Gu, M. F. 2008, CaJPh, 86, 675
Heuer, K., Foster, A. R., & Smith, R. 2021, ApJ, 908, 3
Heyl, J., Caiazzo, I., Hoffman, K., et al. 2019, BAAS, 51, 175
Hitomi Collaboration, Aharonian, F., Akamatsu, H., et al. 2016, Natur, 535, 117
Hitomi Collaboration, Aharonian, F., Akamatsu, H., et al. 2017, Natur, 551, 478
Hitomi Collaboration, Aharonian, F., Akamatsu, H., et al. 2018a, PASJ, 70, 10
Hitomi Collaboration, Aharonian, F., Akamatsu, H., et al. 2018b, PASJ, 70, 11
Hitomi Collaboration, Aharonian, F., Akamatsu, H., et al. 2018c, PASJ, 70, 12
Kaastra, J. S., Gu, L., Mao, J., et al. 2017, JInst, 12, C08008
Kaastra, J. S., Mewe, R., & Nieuwenhuijzen, H. 1996, 11th Colloq. on UV and X-ray Spectroscopy of Astrophysical and Laboratory Plasmas, 411
Kaastra, J. S., Paerels, F. B. S., Durret, F., Schindler, S., & Richter, P. 2008, SSRv, 134, 155
Kaastra, J. S., Raassen, A. J. J., de Plaa, J., & Gu, L. 2020, SPEX X-ray Spectral Fitting Package, v3.06.01, Zenodo, doi:10.5281/zenodo.4384188
Kisielius, R., Berrington, K. A., & Norrington, P. H. 1996, A&AS, 118, 157
Landini, M., & Monsignori Fossi, B. C. 1970, A&A, 6, 468
Li, S., Yan, J., Li, C. Y., et al. 2015, A&A, 583, A82
Lodders, K., Palme, H., & Gail, H. P. 2009, Solar System, Landolt-Börnstein - Group VI Astronomy and Astrophysics, Vol. 4B (Berlin: Springer), 712
Malespin, C., Ballance, C. P., Pindzola, M. S., et al. 2011, A&A, 526, A115
Mao, J., & Kaastra, J. 2016, A&A, 587, A84
Mao, J., Kaastra, J. S., Guainazzi, M., et al. 2019, A&A, 625, A122
Mewe, R. 1972, SoPh, 22, 459
Mitsuda, K., Kelley, R. L., Akamatsu, H., et al. 2014, Proc. SPIE, 9144, 91442A
Nandra, K., Barret, D., Barcons, X., et al. 2013, arXiv:1306.2307
Nussbaumer, H., & Storey, P. J. 1978, A&A, 64, 139
Ogorzalek, A., Zhuravleva, I., Allen, S. W., et al. 2017, MNRAS, 472, 1659
Paerels, F. B. S., & Kahn, S. M. 2003, ARA&A, 41, 291
Phillips, K. J. H., Sylwester, J., Sylwester, B., & Landi, E. 2003, ApJL, 589, L113
Porquet, D., Dubau, J., & Grosso, N. 2010, SSRv, 157, 103
Raymond, J. C. 2005, in AIP Conf. Proc. 774, X-ray Diagnostics of Astrophysical Plasmas: Theory, Experiment, and Observation, ed. R. Smith (Melville, NY: AIP), 15
Raymond, J. C., & Smith, B. W. 1977, ApJS, 35, 419
Robicheaux, F., Gorczyca, T. W., Pindzola, M. S., & Badnell, N. R. 1995, PhRvA, 52, 1319
Sampson, D. H., Goett, S. J., & Clark, R. E. H. 1983, ADNDT, 29, 467
Sazonov, S. Y., Sunyaev, R. A., & Cramphorn, C. K. 2002, A&A, 393, 793
Shah, C., Hell, N., Hubbard, A., et al. 2021, ApJ, 914, 34
Si, R., Li, S., Wang, K., et al. 2017, A&A, 600, A85
Smith, R. K., Abraham, M. H., Allured, R., et al. 2016, Proc. SPIE, 9905, 99054M
Smith, R. K., Brickhouse, N. S., Liedahl, D. A., & Raymond, J. C. 2001, ApJL, 556, L91
Tashiro, M., Maejima, H., Toda, K., et al. 2018, Proc. SPIE, 10699, 1069922
Urdampilleta, I., Kaastra, J. S., & Mehdipour, M. 2017, A&A, 601, A85
Whiteford, A. D. 2005, Helium-like Ions, OPEN-ADAS, https://open.adas.ac.uk/
Whiteford, A. D., Badnell, N. R., Ballance, C. P., et al. 2001, JPhB, 34, 3179
Xu, H., Kahn, S. M., Peterson, J. R., et al. 2002, ApJ, 579, 600
Yamada, S., Ohashi, T., Ishisaki, Y., et al. 2018, JLTP, 193, 1016
Zhang, S., Wang, Q. D., Ji, L., et al. 2014, ApJ, 794, 61